JGR Earth Surface

RESEARCH ARTICLE
10.1029/2019JF005446

Sea Level Rise Will Drive Divergent Sediment Transport Patterns on Fore Reefs and Reef Flats, Potentially Causing Erosion on Atoll Islands

James F. Bramante[1], Andrew D. Ashton[1], Curt D. Storlazzi[2], Olivia M. Cheriton[2], and Jeffrey P. Donnelly[1]

[1]Department of Geology and Geophysics, Woods Hole Oceanographic Institution, Woods Hole, MA, USA, [2]Pacific Coastal and Marine Science Center, U.S. Geological Survey, Santa Cruz, CA, USA

Key Points:
- Relative to sea level rise, wave climate change projected for 2100 CE has negligible influence on cross-shore sediment transport rates
- On fore reefs where most carbonate sediment is produced, sea level rise decreases potential onshore sediment transport rates
- On reef flats, sea level rise increases wave skewness and decreases wave asymmetry, increasing potential onshore sediment transport rates

Supporting Information:
- Supporting Information S1

Correspondence to:
J. F. Bramante,
jbramante@whoi.edu

Citation:
Bramante, J. F., Ashton, A. D., Storlazzi, C. D., Cheriton, O. M., & Donnelly, J. P. (2020). Sea level rise will drive divergent sediment transport patterns on fore reefs and reef flats, potentially causing erosion on atoll islands. *Journal of Geophysical Research: Earth Surface*, *125*, e2019JF005446. https://doi.org/10.1029/2019JF005446

Received 21 NOV 2019
Accepted 15 SEP 2020
Accepted article online 25 SEP 2020

Abstract Atoll reef islands primarily consist of unconsolidated sediment, and their ocean-facing shorelines are maintained by sediment produced and transported across their reefs. Changes in incident waves can alter cross-shore sediment exchange and, thus, affect the sediment budget and morphology of atoll reef islands. Here we investigate the influence of sea level rise and projected wave climate change on wave characteristics and cross-shore sediment transport across an atoll reef at Kwajalein Island, Republic of the Marshall Islands. Using a phase-resolving model, we quantify the influence on sediment transport of quantities not well captured by wave-averaged models, namely, wave asymmetry and skewness and flow acceleration. Model results suggest that for current reef geometry, sea level, and wave climate, potential bedload transport is directed onshore, decreases from the fore reef to the beach, and is sensitive to the influence of flow acceleration. We find that a projected 12% decrease in annual wave energy by 2100 CE has negligible influence on reef flat hydrodynamics. However, 0.5–2.0 m of sea level rise increases wave heights, skewness, and shear stress on the reef flat and decreases wave skewness and shear stress on the fore reef. These hydrodynamic changes decrease potential sediment inputs onshore from the fore reef where coral production is greatest but increase potential cross-reef sediment transport from the outer reef flat to the beach. Assuming sediment production on the fore reef remains constant or decreases due to increasing ocean temperatures and acidification, these processes have the potential to decrease net sediment delivery to atoll islands, causing erosion.

1. Introduction

Anthropogenic climate change over the coming centuries threatens the habitability of atoll reef islands and is expected to alter island sediment transport dynamics. Predictions of atoll reef island response to climate change have relied on extrapolation from recent trends in remotely sensed images and examination of reef- and island-building timelines in the geological record (e.g., McLean & Kench, 2015). However, the processes governing sediment production, transport, and fate on atolls remain poorly understood. On one hand, this is because atolls are ecogeomorphic regions featuring strong feedbacks between biota and hydrodynamic processes, with beds consisting often of a mix of a consolidated carbonate bed and loose sediment. In terms of our process understanding, the hydrodynamics of shallow reef flats is complex, with nonlinear-wave motions such as asymmetry, skewness, and acceleration that may affect predictions of sediment transport. Here we focus on Kwajalein Island, in the Republic of the Marshall Islands (RMI), using wave and hydrodynamic modeling to investigate how changes in wave climate and increased sea level driven by climate change are likely to alter cross-shore sediment transport and, thus, affect the sediment budgets of ocean-facing reef island beaches.

Atoll reef islands are dynamic landforms typically composed of unconsolidated carbonate sediment that reach an elevation of no more than 2–5 m above mean sea level (AMSL) (Woodroffe, 2008). Reef islands are distributed nonuniformly on the annular, intertidal carbonate platforms of mid-ocean coral atolls and are vulnerable to oceanic natural hazards such as tropical cyclones and tsunamis, which can form or erode islands entirely (Ford & Kench, 2015). Due to their low elevation, unconsolidated composition, and natural hazard risk, atoll reef islands and their human inhabitants are considered particularly vulnerable to hazards caused by anthropogenic climate change.

The International Panel on Climate Change (IPCC) forecasts climate change-associated global sea level rise (SLR) of up to 1 m by 2100 (Church et al., 2013). The sea level fingerprint from melting ice sheets could cause SLR in the tropical Marshall Islands to exceed 2 m under the same IPCC emissions scenarios (Kopp et al., 2017). Currently, the fringing fore reefs and reef flats that separate reef islands from the open ocean dissipate most waves before they reach island shorelines (Quataert et al., 2015). However, SLR will allow larger waves to impinge on the shoreline, resulting in more frequent flooding of atoll reef islands (Cheriton et al., 2016; Merrifield et al., 2014; Storlazzi, Shope, et al., 2015); episodic flooding of the islands and saltwater intrusion through the karstified atoll platform can disrupt subsistence agriculture and the freshwater lenses on which it depends (Hoeke et al., 2013; Oberle et al., 2017; Storlazzi et al., 2018).

As global atmospheric circulation patterns change with climate, so too will the directional distribution and height of waves incident on fringing reefs and island shorelines (Shope et al., 2016). Additionally, climate change is projected to increase the frequency and intensity of tropical cyclones (e.g., Zhang et al., 2017), which, in combination with SLR, will result in more frequent and disruptive modification of atoll reef island morphology (Ford & Kench, 2016). Little is known about the likely effect of changing wave forcing on atoll island morphological change. Previous modeling studies have demonstrated that modest changes to wave climate affect longshore transport gradients on atoll islands (Shope et al., 2017; Shope & Storlazzi, 2019) but have not addressed their likely effects on cross-shore transport. Determining the influence of changing wave climate on transport processes, especially relative to sea level rise, will inform efforts to mitigate and adapt to climate change hazards.

The majority of atoll reef islands in the Pacific formed during or after a sea level highstand that lasted 5.0–1.5 kya, during which sea level was 1–3 m AMSL in the equatorial Pacific Ocean (Dickinson, 2009; Grossman et al., 1998). With the premise that few modern islands existed on atoll platforms during rapid postglacial SLR and the sea level highstand, it has been proposed that climate change-driven SLR could cause erosion of atoll reef island shorelines and eventually lead to the permanent removal of entire islands from atoll rims (Dickinson, 1999, 2009). This potential risk has been underscored by reports of recent erosion of reef island ocean-facing shorelines in the Solomon Islands (Albert et al., 2018) and elsewhere (Webb & Kench, 2010), often implicitly attributed to erosion through direct offshore transport (McLean & Kench, 2015). However, research using mid-Holocene histories of atoll reef islands as proxies for island response to higher sea level demonstrate that some islands formed, grew, and remained stable under the sea level highstand (Kench et al., 2012, 2014; Woodroffe, 2008). Furthermore, under recent, accelerating SLR (0.013 mm year^{-2}; Church & White, 2006), many islands have expanded in planform area (McLean & Kench, 2015). In the Marshall Islands in particular, islands have increased in planform area over the past 70 years, although this trend has reversed for many islands since the 1970s (Ford, 2013; Ford & Kench, 2015). The absence of a consistent shoreline response to modern rates of SLR on atoll islands prevents extrapolation of shoreline response to future, accelerated SLR without a better understanding of the sediment production and transport processes maintaining atoll island shorelines.

The specific drivers of observed shoreline changes remain unknown, in part due to the low temporal resolution of the satellite and aerial image record used to track shoreline change (Ford, 2013) and the complexity of atoll island shoreline dynamics. The shorelines of atoll reef islands are dynamic, often responding to variability in wave climate on seasonal and interannual timescales with little to no net change in island area or volume (Dawson & Smithers, 2010; Kench & Brander, 2006; Rankey, 2011). However, in a time-mean sense, the ocean-facing shorelines of atoll reef islands are maintained by a balance in which sediment produced on the fore reef and reef flat is delivered cross shore to the beach and sediment on the beach is redistributed through alongshore transport and moved inland through episodic overwash (Perry et al., 2011; Tuck et al., 2019). The rate of cross-shore sediment input to the shoreline is in turn a function of sediment production on the reef and the hydrodynamic flows that deliver sediment to the shoreline. To investigate the hydrodynamic flows responsible for sediment delivery, we use the concept of potential sediment transport, that is, the expected sediment transport rate assuming an inexhaustible volume of sediment. Shoreline erosion thus occurs due to a sediment budget deficit, which from a balanced initial state can be caused by one or a combination of the following: enhanced net alongshore sediment transport gradients, enhanced overwash, reduced reef sediment production, or reduced potential cross-shore sediment transport.

The processes composing the sediment budgets that maintain island morphology are understudied. In terms of sediment removal from the beach, studies have nearly unanimously predicted greater overtopping as sea

level rises and, thus, inferred increases in atoll overwash frequency over the next century (e.g., Cheriton et al., 2016; Merrifield et al., 2014; Shope et al., 2017; Storlazzi et al., 2018). Additional modeling studies have demonstrated that potential anthropogenic decreases in reef health and, thus roughness, may have similar impacts as SLR (Harris et al., 2018; Quataert et al., 2015; Sheppard et al., 2005). Recent wave flume and wave tank studies suggest that reef island morphodynamics exhibit a negative feedback relationship with overtopping, in which island freeboard elevation keeps up with SLR through overwash-induced lagoonward migration and vertical accretion (Tuck et al., 2019), previously hypothesized with geometric arguments (Kench & Cowell, 2001). Additionally, Shope et al. (2017) and Shope and Storlazzi (2019) examined how changing wave climate and SLR may affect net alongshore transport on atoll reef islands and predict that changing wave direction and SLR-enhanced alongshore transport gradients will redistribute sediment along ocean-facing and lagoon shorelines, resulting in net erosion of windward, ocean-facing shorelines.

Similar to other nearshore environments, the cross-shore transport component of the sediment balance is particularly poorly understood. A wave flume experiment found that cross-shore sediment transport resulted from skewness and asymmetry of both high- and low-frequency waves, with the relative dominance of these contributors varying over the reef profile (Pomeroy et al., 2015). Additionally, recent field studies have highlighted the problems with applying conventional sediment transport flux equations to reef environments (Pomeroy et al., 2017, 2018). Recent hydrodynamic modeling using hypothetical reef flat geometries indicates that internal feedbacks can control reef flat elevations and widths for a given constant sea level (Ortiz & Ashton, 2019).

In this study, we quantify the impact of SLR and wave climate change on atoll island hydrodynamics and potential cross-shore sediment transport. First, we calibrate the phase-resolving hydrodynamic wave model, XBeach, for Kwajalein Atoll's windward reef and verify the model's accuracy. Next, we use the XBeach model to quantify the response of bottom shear stress and inferred potential sediment transport to both wave climate change and SLR. We then provide in-depth analysis of hydrodynamics maintaining atoll island sediment budgets.

2. Study Area

Kwajalein Atoll is a large coral atoll in the Ralik island chain of RMI, in the central North Pacific (Figure 1). It has one of the largest lagoons in the world with a surface area of over 2,300 km^2 (Sugerman, 1972). The lagoon is surrounded by a 300–1,500 m wide intertidal reef platform, broken periodically by deep channels connecting the ocean to the lagoon. Beyond the reef platform is a fore reef consisting of coral-algal boundstone and unconsolidated or weakly consolidated sediment (Hunt et al., 1995).

Kwajalein Atoll is partially sheltered from Pacific Ocean basin-wide wave energy by its position within the Marshall Islands. Wave generation by trade winds incident on Kwajalein Atoll is fetch limited by the Ratak island chain 250–300 km to the east, lowering mean incident wave height relative to that experienced by atolls in the eastern chain (Figure 1a). Similarly, northern RMI atolls block some swell generated by extratropical cyclones from reaching Kwajalein Atoll, but northerly swell waves occasionally flood islands on the atoll (Hoeke et al., 2013; Quataert, 2015). Tropical cyclones locally generate large waves, but historically, these large wave events have been rare. Twelve storms recorded in the International Best Track Archive for Climate Stewardship (IBTrACS) have come within 100 km of Kwajalein Island since 1850. At least two of those tropical cyclones, Typhoons Roy (1988) and Zelda (1991), generated waves that overtopped the ocean-facing beach ridges on Kwajalein Island and nearby Ebeye Island (Joint Typhoon Warning Center (JTWC), 1988, 1991). Colonial records also indicate that a tropical cyclone inundated Kwajalein Atoll in 1875, reportedly sweeping the island of all inhabitants (Spennemann, 2004).

3. Wave Model Training and Evaluation

3.1. Wave Model Setup

To examine the influence of sea level rise on cross-shore sediment transport, we used XBeach to model wave propagation and associated hydrodynamics across Kwajalein's fringing reef. XBeach is a nonlinear shallow water equation solver forced by time-varying spectral wave and flow boundary conditions (Smit et al., 2010) and has been tested and applied to fringing reef environments similar to Kwajalein

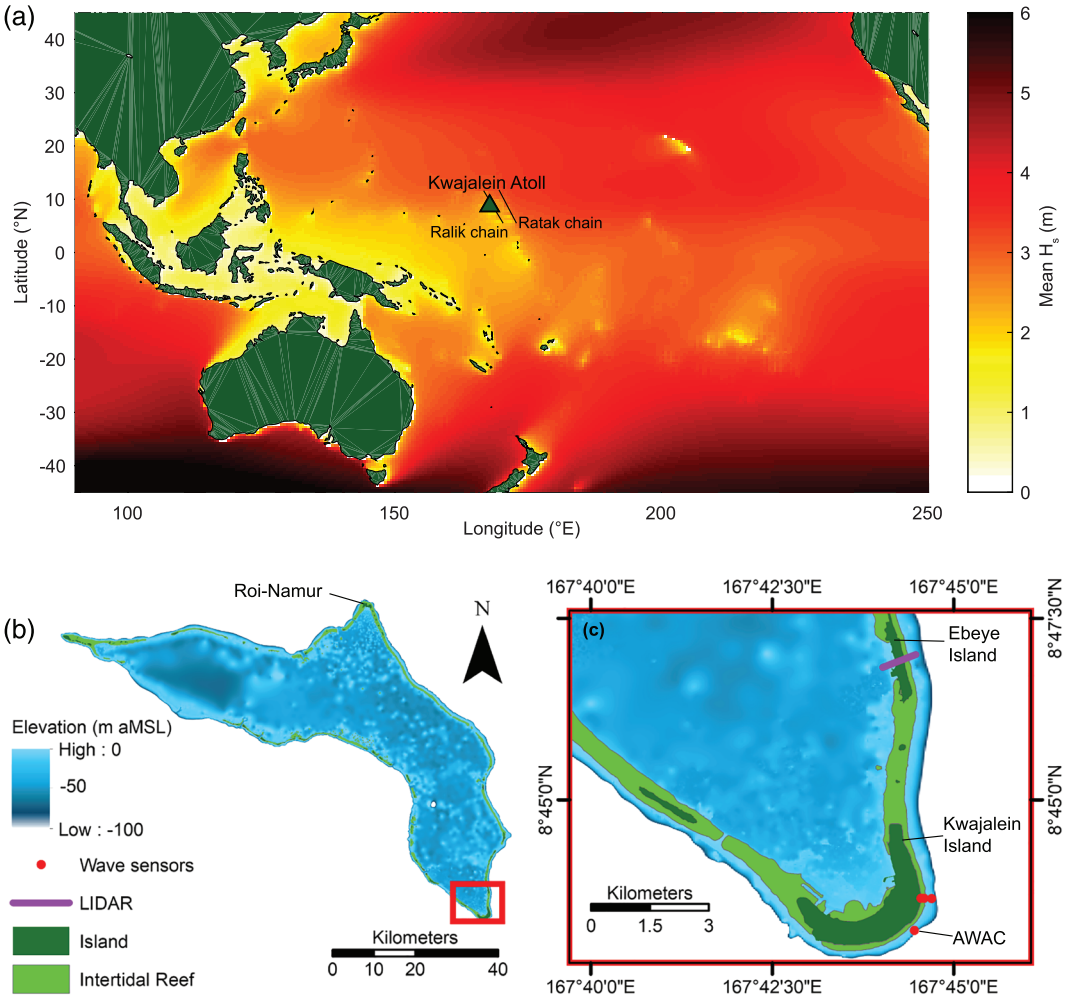

Figure 1. Maps of the study area showing (a) mean significant wave height (H_s) from the CFSRR reanalysis, (b) Kwajalein atoll bathymetry, and (c) the location of LIDAR data and wave sensors used to construct and evaluate the XBeach model.

Island (Lashley et al., 2018; Quataert et al., 2015). We ran XBeach in 1-D nonhydrostatic mode, such that the model resolved both high- and low-frequency wave motions across a cross-shore transect of the reef. Previous field and experimental studies have demonstrated that wave nonlinearity and low-frequency wave motions drive cross-shore sediment transport on shallow reefs (Pomeroy et al., 2015, 2018). Resolving these processes is computationally intensive but is necessary for accurate projections of cross-shore transport. In choosing to use a 1-D model, we are neglecting effects such as wave refraction and diffraction that require explicit 2-D modeling and which can alter the incident wave field, especially on the midreef flat. We address the impact these 2-D processes may have on our results in section 6.

When compared with low-friction laboratory flume models of fringing reefs (similar in form to atoll reefs), XBeach accurately simulates wave height, water level, and runup with default model parameters (Lashley et al., 2018). However, when used to simulate rough fringing reefs, XBeach requires tuning of a coefficient of friction (c_f) that is used to calculate total bottom shear stress (τ_t, Nm^{-2}) as

$$\tau_t = \rho c_f u|u| \tag{1}$$

where ρ is water density ($\mathrm{kg\ m}^{-3}$) and u is cross-shore water velocity ($\mathrm{m\ s}^{-1}$) (Smit et al., 2010).

To tune c_f and verify that our model produced realistic results, we used data from an array of wave sensors deployed across the fringing reef at Kwajalein Island. One Nortek acoustic wave and current (AWAC)

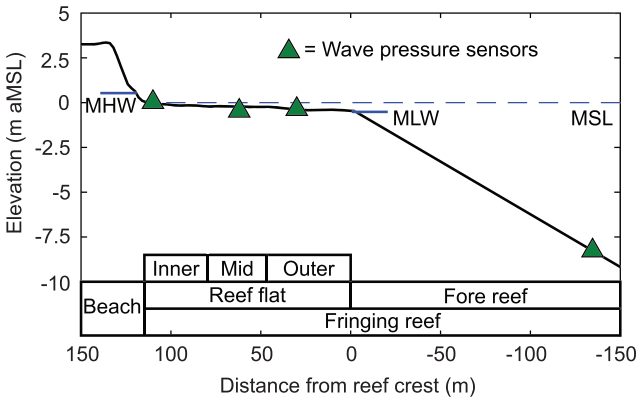

Figure 2. Model bathymetry, tidal datum, the location of wave sensors on Kwajalein Island's fringing reef, and identification of reef zones.

profiler and four pressure sensors (RBR Virtuosos) were deployed on the eastern fringing reef of Kwajalein Island from 9 November 2013 to 19 April 2014 (Figure 1). The AWAC and pressure sensors were set to sample for 2,048 s every hour at 1 and 2 Hz, respectively. Sensors were geolocated using postprocessed GNSS, and sensor elevations on the reef flat were surveyed to the Kwajalein Island tide gauge and calculated relative to local mean sea level during deployment (Figure 2). For model tuning and verification, 17 days of sensor data (8–25 March 2014) were selected to cover the transition from neap tide to spring tide. Waves during this interval were characteristic of trade wind waves and were representative of the entire deployment with a mean (± standard deviation) $H_s = 1.5$ (±0.5) m, $T_p = 7.7$ (±1.75) s, and $\theta_{mean} = 97°$ (±9°).

We tuned model c_f by forcing the model with 48 hr (13–15 March 2014) of AWAC data transformed to JONSWAP spectra defined by hourly H_s, T_p, and θ_{mean}. We then compared hourly H_s and water surface elevation between the model and sensors on the fore reef and reef flat using root-mean-square error (RMSE) and the Pearson product-moment correlation coefficient (r) as objective functions. Hourly H_s was calculated from 2,048 s of sensor or model data as

$$H_s = 4\sqrt{\int_{f_1}^{f_2} S(f)df} \tag{2}$$

where f is frequency (Hz), f_1 and f_2 are frequency bounds defining high (0.3–0.04 Hz) or low (0.04–0.001 Hz) frequency waves, and S is the 1-D wave-energy spectrum (m^2 s) calculated using the Welch's modified periodogram method with a Hanning window of 1,024 s. The tuning data included the largest recorded wave height of the deployment at $H_s = 2.85$ m and tides of intermediate magnitude. The remaining 15 days of selected wave data were used to verify model accuracy over a broader range of wave and tide conditions.

High-resolution bathymetric data were unavailable along the transect of wave sensors fronting Kwajalein Island, so model bathymetry was derived from an airborne LIDAR transect across nearby Ebeye Island (Figure 1c), where reef flat width and fore reef slope are similar to that along the wave sensor transect. The LIDAR data were linearly interpolated to a uniform grid with 0.5 m spatial resolution (Figure 2). Topographical variability on the fore reef was removed as in Quataert et al. (2015) to make results more generalizable, with little impact on model accuracy. Depths were uniformly tied to local mean sea level during deployment by lowering the cross section until it intersected the elevation of the outer reef flat sensor. Sensor locations were matched to grid cells based on their distance from the reef crest. The inner reef flat sensor aligned well with model bathymetry, but the midreef flat sensor was deployed in an anomalous depression and was located 22 cm below model bathymetry (Figure 2). Despite this discrepancy, we used data from all sensors for model evaluation.

3.2. Wave Model Evaluation

After tuning the nonhydrostatic, phase-resolving XBeach wave model with 2 days of hourly wave data, the identified best fit friction coefficient values were similar to c_f values from other published investigations of fringing reefs. The reef flats fronting Kwajalein Island and Roi-Namur are very shallow at low tide, which prevents coral growth and reduces surface roughness on the reef flat relative to the fore reef, requiring separate friction coefficient values for those two regions of the reef (Quataert et al., 2015). The model reproduced wave heights and water levels over the reef most accurately with $c_f = 0.15$ on the fore reef and $c_f = 0.015$ on the reef flat and beach. For a similar reef cross section at Roi-Namur, 82 km northwest of our site, Quataert et al. (2015) optimized XBeach model performance with $c_f = 0.1$ on the fore reef and $c_f = 0.01$ on the reef flat. Kwajalein's fore reef has greater coral cover, and thus roughness, than Roi-Namur, which we assume is consistent with the larger friction coefficient in the optimized model. The reef flat c_f value is less than half that of van Dongeren et al. (2013) for a 2-D hydrostatic model of Ningaloo Reef ($c_f = 0.04$), likely due to the relative smoothness of Kwajalein Island's reef flat.

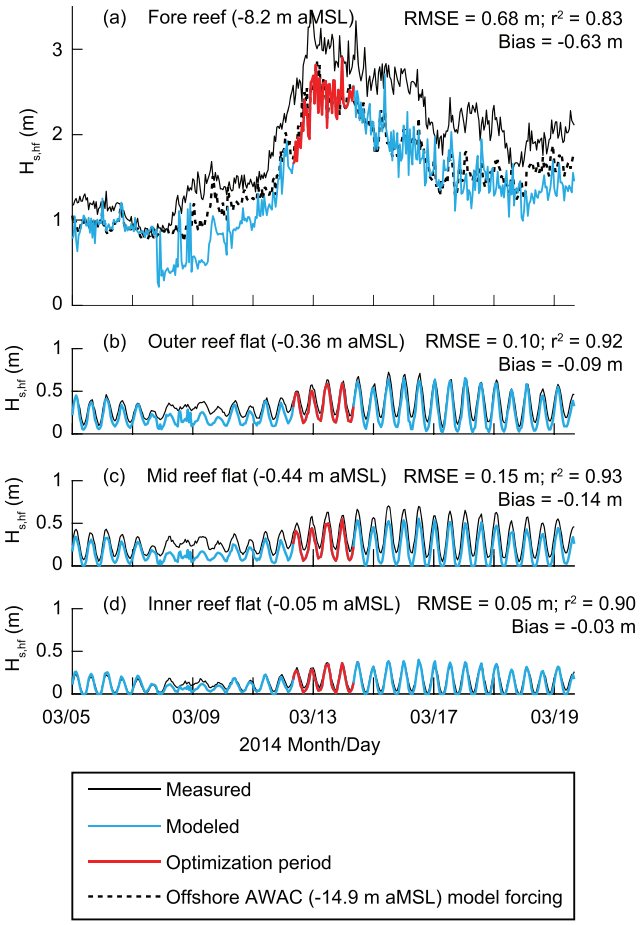

Figure 3. Measured and modeled high frequency significant wave heights ($H_{s,hf}$) on the (a) fore reef, (b) outer reef flat, (c) midreef flat, and (d) inner reef flat. Sensor elevations are displayed in parentheses. $H_{s,hf}$ recorded at the offshore AWAC is plotted in (a). The objective functions, RMSE, r^2, and mean bias (model minus observations) report the correspondence between measured and modeled data, excluding the optimization period.

Wave refraction and blocking in the vicinity of the offshore AWAC possibly resulted in discrepancies between modeled and measured wave heights across the fringing reef. Modeled wave heights on the fore reef consistently matched wave heights at the offshore AWAC used to force the model (Figure 3a) but underestimated wave heights measured by the fore-reef pressure sensor. The offshore AWAC is located on a cross-shore transect roughly 45° clockwise from the transect of wave pressure sensors on the reef flat (Figure 1c). The mean wave direction, θ_{mean}, at the offshore AWAC was 111° during the first 72 hr of model verification and then shifted northerly to 94° for the next 2 weeks. As incident θ_{mean} shifted, refraction along the curving coast between the two sensors would have decreased wave heights at the AWAC relative to the fore reef sensor. Additionally, the eastern sensor transect may have recorded oblique northerly waves that were subsequently blocked by the reef before they could reach the AWAC. These discrepancies in forcing potentially contributed to our model underestimating wave heights and water level across the fringing reef. This discrepancy illustrates one of the potential weaknesses of using a 1-D model.

Comparison of model results to the midreef flat sensor reveals considerable underprediction of wave heights but better agreement in water surface elevation (Figures 3 and 4). We speculate that the deeper water between the inner-reef flat and midreef flat sensors depressed frictional dissipation of wave energy relative to the model bathymetry, resulting in higher measured wave heights but lower measured water level. Additionally, wave refraction over the reef crest to the southwest may have introduced additional wave energy to the midreef flat, which would not have been captured by the 1-D modeling approach.

Despite some discrepancies resulting from suboptimal model bathymetry and forcing, our model accurately simulates the important wave transformation processes occurring across the fringing reef. Incident high-frequency waves break on the shallow fore reef and reef crest, resulting in much smaller, tidally modulated wave heights on the reef flat relative to the fore reef (Figure 3). High-frequency wave heights, $H_{s,hf}$, decrease across the reef flat, where friction contributes to wave dissipation. Break-point forcing on the fore reef (Becker et al., 2016; Symonds et al., 1982) generates low-frequency waves on the outer reef flat that are larger than those over the fore reef (Figure 4). For higher water levels and also for larger fore-reef waves, low-frequency wave heights, $H_{s,lf}$, increase across the reef flat (Cheriton et al., 2016; Gawehn et al., 2016).

The model tends to underestimate reef flat water levels at low tide or when incident waves are large (Figure 4), a discrepancy that is consistent with previous studies applying 1-D XBeach nonhydrostatic models to both idealized reefs in laboratory flumes (Lashley et al., 2018) and the reef at Roi-Namur on the northern side of Kwajalein Atoll (Quataert et al., 2015). Lashley et al. (2018) demonstrated that this water level bias likely occurs because the model does not account for wave roller contributions to kinetic energy and that this bias is common among models making shallow water or Boussinesq assumptions. Our simulations verify these earlier findings and indicate that the model is suitable to examine changes in wave-driven hydrodynamics with varying wave climate and sea level.

4. Data and Methods

4.1. Wave Climate Analysis

To examine changes in wave climate we used Wavewatch III® forecasts driven by four general circulation models (GCMs) from the Coupled Model Intercomparison Project 5 (CMIP5) (Storlazzi, Elias, et al., 2015). The four GCMs used were the Beijing Climate Center (BCC) Community Systems Model 1.1, Institute for

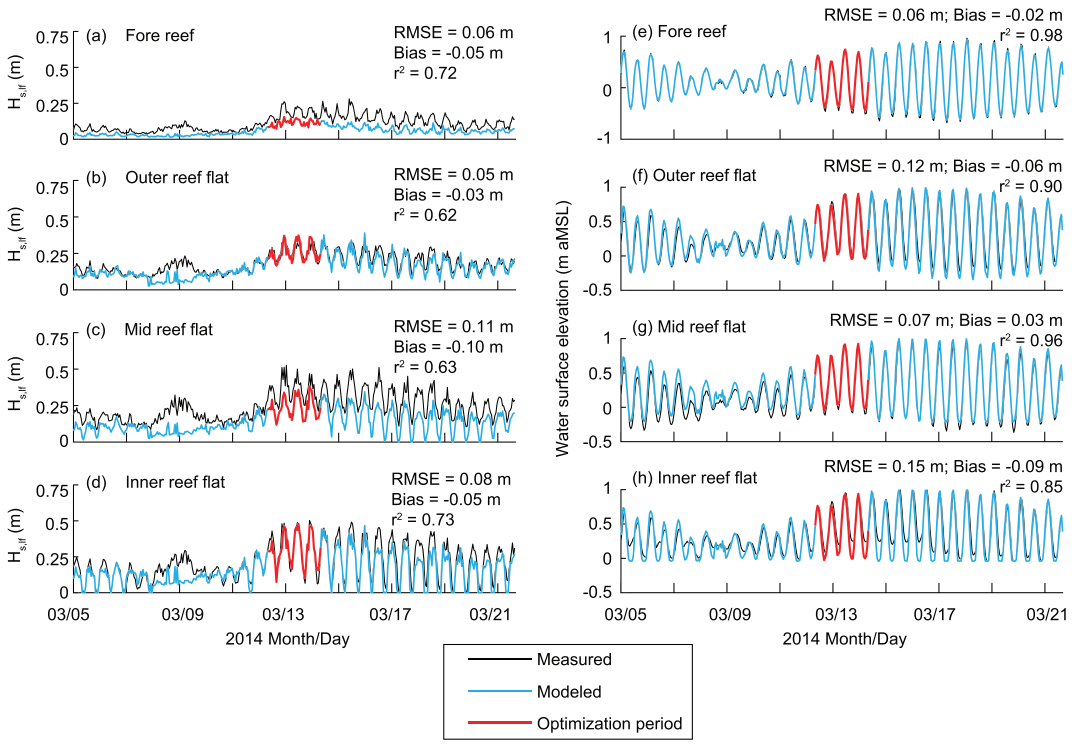

Figure 4. Measured and modeled (a–d) low-frequency significant wave height ($H_{s,lf}$) and (e–h) hourly mean water surface elevation. The objective functions, RMSE, r^2, and mean bias (model minus observations) report the correspondence between measured and modeled data, excluding the optimization period.

Numerical Mathematics Coupled Model 4 (INMCM), Model for Interdisciplinary Research on Climate 5 (MIROC), and the Geophysical Fluid Dynamics Laboratory Earth Systems Model 2M (GFDL). For each GCM, waves were simulated for two time periods: historical (1976–2005), mid-21st century (2026–2045), and late 21st century (2085–2100). To capture the most extreme potential changes in wave climate, we examined only GCM results for the Representative Concentration Pathway 8.5 (RCP8.5) climate scenario representing unchecked carbon emissions and resultant radiative forcing over the 21st century. The GCM forecasts generated wave characteristics at 1.00° × 1.25° spatial resolution; we used data extracted from the grid cell centered at (8.75°N, 167.75°E). For each of the time periods, the wave data from all four GCMs were combined to create a model ensemble.

To quantitatively describe the wave climate, we separated waves into classes using *k*-means unsupervised classification (Xu & Wunsch, 2005) of linear wave energy density, T_p, and θ_{mean}. The number of classes produced, *k*, was chosen as that which explained 90% of the variance in the three wave characteristics. Prior to classification, the values of the three wave characteristics were transformed to *z* scores so their values would all be of the same order of magnitude. This classification procedure was performed separately for each time period (historical, mid-21st century, and late 21st century) and each data set.

4.2. Model Scenarios and Statistics

To determine the potential impact of wave climate change on cross-reef hydrodynamics and sediment transport, we ran the XBeach model under six scenarios. First, as a baseline, we forced the model with every wave class from the historical GCM ensemble (Historical). Second, we forced the model with every wave class from the late 21st century GCM ensemble, with sea level held at historical levels (Wave Climate Change). Finally, we forced the model with the historical GCM ensemble wave classes for each of four SLR magnitudes: +0.5, +1.0, +1.5, and +2.0 m relative to local MSL.

The SLR scenarios considered in this study cover the range of projected SLR by 2100 for Kwajalein Island. The IPCC Fifth Assessment Report (AR5) projected likely global SLR by 2100 of 0.74 (0.53) m for RCP 8.5

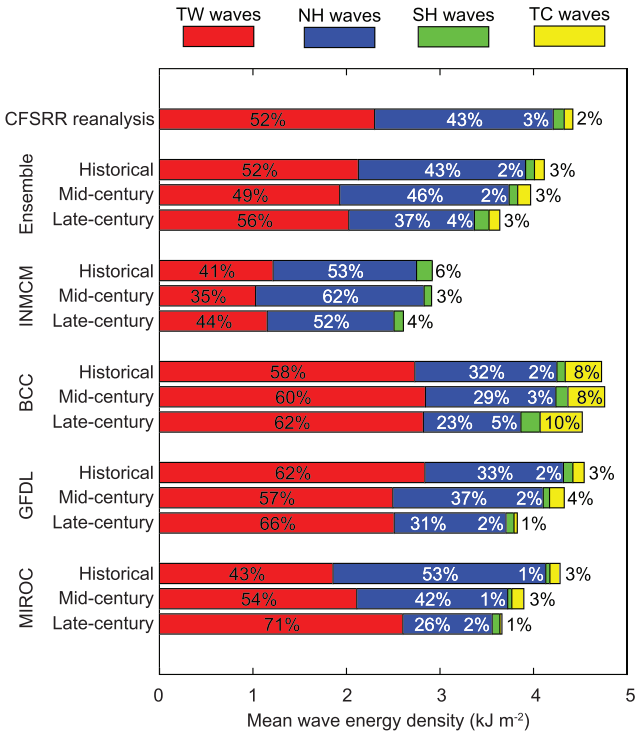

Figure 5. Mean wave energy density categorized by primary wave source, data set, and time period. Percentages indicate the proportion of mean wave energy density accounted for by each wave source within a time period. The Climate Forecast System Reanalysis Reforecast (CFSRR) reanalysis results are discussed in SI Wave Climate Results.

(4.5) (Church et al., 2013). However, due to feedbacks between water storage, gravity, lithospheric loading, and planetary rotation, SLR can vary widely across the globe for a given increase in ocean volume (Hsu & Velicogna, 2017; Mitrovica et al., 2009). This variability, or sea level fingerprint, results in greater forecast SLR rates in the tropics relative to the rest of the globe. After accounting for the sea level fingerprint and incorporating expert opinion into a statistical model of SLR, Kopp et al. (2014) forecast mean (90% confidence interval) SLR at Kwajalein Island by 2100 CE of +0.89 (+0.42–1.58) m for RCP8.5 and +0.67 (+0.31–1.21) m for RCP4.5. However, these forecasts were recently updated with physical modeling of ice sheet dynamics, producing mean SLR at Kwajalein Island of +1.72 (+1.00–2.93) m for RCP8.5 and +1.07 (+0.54 – 1.89) m for RCP4.5 (Kopp et al., 2017). Thus, Kwajalein Island is expected to experience at least +0.5 m and up to nearly +2 m of SLR by 2100.

Applying the above SLR scenarios in our experiment makes the implicit assumption that reef accretion will be negligible relative to SLR by 2100. The optimal reef flat vertical accretion rates in the Holocene before human-induced thermal stress, acidification, and land-based pollution were on the order of 1–6 mm/year in high-energy areas such as atoll fore reefs (Montaggioni, 2005). Climate change-driven bleaching and ocean acidification will have reduced these rates from their Holocene optimum (Hoegh-Guldberg, 1999; Pandolfi et al., 2011). Additionally, the elevation of Kwajalein's fringing reef flat between MSL and low tide (Figure 2) will likely create a lag between SLR and colonization of the reef flat surface by framework corals, delaying accretion. Thus, relative SLR is unlikely to deviate from the range of the above SLR projections, and the model does not consider feedbacks between predicted hydrodynamics and island or reef morphodynamics.

Using 4,096 s long, 1 Hz time series of wave velocity and water depth after 5 hr of model spin-up for each wave class, high-frequency wave heights ($H_{s,hf}$) and low-frequency wave heights ($H_{s,lf}$) were calculated from the output water depth time series using conventional spectral analysis as in section 3.1. We then separated wave velocity into low- and high-frequency components using ensemble empirical mode decomposition (EEMD; Wu & Huang, 2009). EEMD uses an iterative peak detection and curve fitting analysis to separate a discrete time series into a number of intrinsic mode functions (IMFs), containing periodic components of the signal, with a nonperiodic residual. The individual IMFs and residual do not share information, such that they can be summed linearly to reproduce the original time series (Huang & Wu, 2008). The IMFs tend to contain information from within narrow frequency bands but do not explicitly account for signal frequency. Thus, low-frequency IMFs can be combined to reproduce the highly nonlinear and irregular low-frequency wave shapes found on reef flats more accurately than conventional band-pass filters (Gawehn et al., 2016). We used EEMD to decompose each velocity time series into 10 IMFs and then applied the Hilbert-Huang Transform (Huang & Wu, 2008) to determine the time-dependent frequency content of each IMF. An IMF was classified as low frequency if its mean frequency fell below 0.05 Hz (>20 s wave period). We then constructed the high-frequency component (u_{hi}) by summing all high frequency IMFs with the EEMD residual and the low-frequency component (u_{lo}) by summing the remaining IMFs.

Distributions of shear stresses were built through bootstrap sampling of model results from all of the wave classes. The entirety of each water velocity time series was included multiple times according to the proportion of the year for which its wave class accounted. For example, all model output from a wave class incident on Kwajalein Island 0.1% of the year would be included once, while all model output from a wave class accounting for 30% of the year would be included 300 times. The resulting bootstrapped distributions had a total sample size of $n = 4.01 \times 10^7$. Shear stress was then calculated using Equation 7 and a probability density function (PDF) estimated from the full samples.

To determine the influence of SLR and wave climate change on wave nonlinearity and determine how those changes influence sediment transport, we diagnosed wave skewness (S_u) using the third-order moment of water velocity and asymmetry (A_u) using the third-order moment of the Hilbert transformation of water velocity (Ruessink et al., 2012):

$$S_u = \overline{u_{hi}^3}/\sigma_u^3 \tag{3}$$

$$A_u = \overline{H(u_{hi})^3}/\sigma_u^3 \tag{4}$$

where u_{hi} is the high frequency component of velocity, σ_u is the standard deviation of that component, $H()$ is the Hilbert transform, and the overbar represents time averaging, both calculated over an entire model output time series.

4.3. Calculating Potential Sediment Transport

To quantify potential net sediment transport rates and their response to changing wave climate and SLR, we use empirical expressions for bedload flux and suspended transport velocity. We estimated potential bedload transport rates using the general sediment bedload flux equation of Nielsen and Callaghan (2003):

$$q_{b,j} = A_2 \frac{\sqrt{\tau_b}\tau_{e,j}}{g\rho^{\frac{3}{2}}(s-1)}, \tag{5}$$

$$\tau_{e,j} = \frac{\tau_b}{|\tau_b|}\max\left(0, |\tau_b| - \tau_{c,j}\right), \tag{6}$$

where q_b is volumetric bedload flux per unit width ($m^2\ s^{-1}$), j is a subscript denoting different grain sizes, τ_b is bed shear stress ($N\ m^{-2}$), τ_e is excess bed shear stress ($N\ m^{-2}$), g is gravitational acceleration ($m\ s^{-2}$), s is the sediment specific gravity, $A_2 = 12$ is an empirical constant, and τ_c is a critical shear stress ($N\ m^{-2}$) threshold above which sediment is mobilized. When Equation 5 is calculated using instantaneous shear stress and then phase averaged, it produces accurate estimates of net bedload flux for both currents and nonlinear waves on plane beds (Nielsen, 2006; Nielsen & Callaghan, 2003; Soulsby & Damgaard, 2005).

We calculated bed shear stress incident on sediment grains using the friction velocity definition of Nielsen and Callaghan (2003):

$$u^* = \sqrt{0.5 f_{2.5}}\left[u(t)\cdot cos\phi_\tau + sin\phi_\tau \frac{1}{\omega_p}\frac{du}{dt}\right], \tag{7}$$

$$\tau_b(t) = \rho u^* |u^*|, \tag{8}$$

where ϕ_τ is a phase lag determining the relative contribution of frictional versus inertial forces to effective friction velocity, ω_p is the peak wave angular frequency ($rad\ s^{-1}$) across a single model time series, and we use a central finite difference formulation to calculate acceleration using model output recorded at 10 Hz. The second term in the brackets of Equation 7 implicitly accounts for two boundary layer processes: thinning of the boundary layer with increasing acceleration, leading to higher shear stress, and acceleration-induced horizontal pressure gradients that exert an additional force on sediment grains in the bed.

Theoretically, ϕ_τ represents a phase lag between velocity and shear stress. However, calibration with empirical and field experimental results suggest that in practice ϕ_τ takes values larger than phase lags that have been measured for smooth and rough beds (Nielsen, 2006). The discrepancy between the calibrated and theoretical values is due in part to the influence of the acceleration-induced horizontal pressure gradients, which are 90° out of phase with velocity (Nielsen & Callaghan, 2003). Nielsen and Callaghan (2003) calculated a best-fit value of $\phi_\tau = 40°$ from one set of flume experiments, with later analysis finding that the best-fit value of ϕ_τ decreased with increasing wave period and grain size (Nielsen, 2006). More recently, Equation 7 was calibrated with $\phi_\tau = 20°$ to replicate the morphological evolution of a mixed sand-gravel environment with natural, longer wave periods than in the previous laboratory experiments (Bergillos et al., 2017). For the

calculations here, we use a base value of $\phi_\tau = 20°$ but also perform a sensitivity test for different values of ϕ_τ, including a case where acceleration is neglected, $\phi_\tau = 0°$.

The skin friction coefficient, $f_{2.5}$, is defined as in Nielsen and Callaghan (2003):

$$f_{2.5} = \exp\left[5.5\left(\frac{2.5D}{\frac{\sqrt{2}}{\omega_p}\sqrt{var\{u(t)\}}}\right)^{0.2} - 6.3\right], \tag{9}$$

where $r = 2.5D$ is a roughness length, D is median sediment grain diameter, and variance in the denominator is calculated over a single model time series.

We estimate the critical shear stress threshold for a given sediment grain size and density using the Shield's parameter:

$$\alpha\theta_c = \frac{\tau_{c,j}}{\rho(s-1)gD_j}, \tag{10}$$

where $\alpha = \sin(\varphi_s + \beta)/\sin(\varphi_s)$ is a correction for the effect of bed slope on mobilization of sediment (Damgaard et al., 1997), $\varphi_s = 32°$ is the static friction angle of submerged sand, and β is local bed slope relative to the direction of flow. For turbulent, steady flow over a horizontal bed, θ_c has been empirically determined to be O(0.05) and varies weakly with the Reynolds number of the flow. Komar and Miller (1975) demonstrated that mobilization thresholds predicted using the Shield's parameter generally hold for oscillatory flow as well, and thus we use $\theta_c = 0.05$ to calculate the critical shear stress for sediment specific gravity of 1.85 and for six median grain sizes: 0.062, 0.5, 2, 16, and 64 mm, which represent the silt/sand, medium/coarse sand, sand/pebble, medium/coarse pebble, and pebble/cobble grain size transitions.

To quantify trends in the net direction of suspended sediment transport with wave climate change and SLR, we estimated the mean velocity of suspended sediment using a representative advection velocity (Pender & Karunarathna, 2013; van Thiel de Vries, 2009) computed from wave statistics:

$$u_{rep}(t) = u_m + u_{lo}(t) + \alpha u_{rms}(t)(S_u(t) - A_u(t)) \tag{11}$$

where u_m is the mean flow velocity (m s^{-1}); u_{lo} is the low frequency wave component of velocity; u_{rms} is the root-mean-square of the high frequency wave component of velocity, u_{hi}; S_u and A_u are the wave skewness and asymmetry defined above such that negative A_u indicates that acceleration is greater in the onshore direction, and $\alpha = 0.1$ is an empirical coefficient whose value was estimated through calibration runs with XBeach (van Thiel de Vries, 2009). To account for possible covariance between low frequency and high frequency wave motions, u_{rms}, S_u, and A_u were all calculated within a 120 s moving window on the u_{hi} time series produced by EEMD.

Equations 5, 7, and 11 were derived and calibrated for low-gradient beds of sediment where the quantity of bed sediment is assumed inexhaustible. However, sediment is relatively sparse on the reef flat and fore reef slope at our site, and thus, the sediment bedload transport flux found with Equation 5 represents an estimate of the maximum potential bedload transport rate, as our model assumes a constant volume of sediment available for transport. We use Equation 11 only to determine the direction of trends in suspended transport rates.

5. Results

5.1. Wave Sources and Forecasts

Despite intermodel variability (supporting information (SI) Wave Climate Results), a trend of decreasing mean wave energy over the next century was consistent across all models (Figure 5). The GCMs unanimously forecast a 4–16% decrease in mean wave energy by 2100, primarily due to a 12–58% reduction in wave energy from Northern Hemisphere extratropical cyclones (NH waves). The ensemble mean forecasts a 12% reduction in mean wave energy over the next century, which is equivalent to one standard deviation of annual mean wave energy in the historical GCM ensemble. In the ensemble mean, wave energy generated

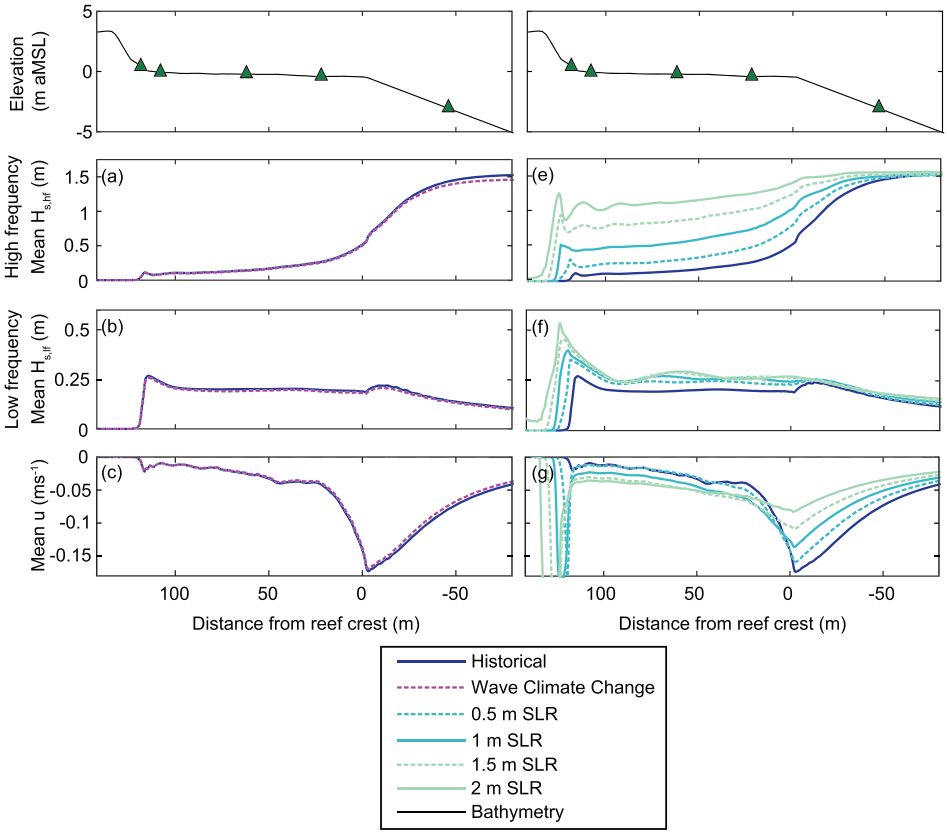

Figure 6. Changes in mean wave and flow characteristics for the six modeling scenarios: Left columns show Historical and Wave Climate Change scenarios, and right columns show the four SLR scenarios with the Historical scenario included for reference. Mean (a, e) $H_{s,hf}$ (0.3–0.04 Hz), (b, f) $H_{s,lf}$ (0.04 – 0.001 Hz), and (c, g) mean cross-shore water velocity. Green triangles indicate locations sampled in Figures 8–13.

by nearby tropical cyclones (TC waves) and Southern Hemisphere extratropical cyclones (SH waves) were forecast to increase slightly and trade wind (TW waves) wave energy to decrease slightly, although there was less intermodel agreement on these changes. The wave directional distributions were forecast to narrow for all wave sources except TC waves and to shift slightly counter-clockwise for all wave sources except TW waves. As the projected changes in wave climate are similar for Majuro and Bikini Atolls (Storlazzi, Elias, et al., 2015), the analysis presented here is likely applicable across the Marshall Islands.

The substantial projected decrease [O(10%)] in wave energy incident on the windward rim of Kwajalein Atoll is consistent across models. This decrease may affect cross-shore sediment transport and sediment budgets that maintain the atoll's reef islands, which is investigated in the following sections.

5.2. Forecasts of Wave Propagation and Shear Stress on the Fringing Reef

5.2.1. Mean Hydrodynamics

After tuning friction coefficients in our XBeach model, we forced it with each of six scenarios representing Historical, Wave Climate Change, and four SLR conditions. Under Historical and Wave Climate Change conditions, most high-frequency wave energy dissipates onshore across the reef through breaking and frictional dissipation (Figure 6a), while $H_{s,lf}$ increases onshore due to breakpoint forcing and the formation of standing waves, progressive-growing waves, and resonant amplification on the reef flat (Gawehn et al., 2016), as shown in Figure 6b. Mean water velocity is offshore over the entire fringing reef, with the strongest flows under breaking waves at the reef crest (Figure 6c). We infer that this mean offshore flow is balanced by onshore-directed wave-induced mass flux as evidenced by the strong negative correlation between mean velocity and mean incident wave dissipation across the reef profile (Pearson's $r = -0.92$, $p < 0.001$).

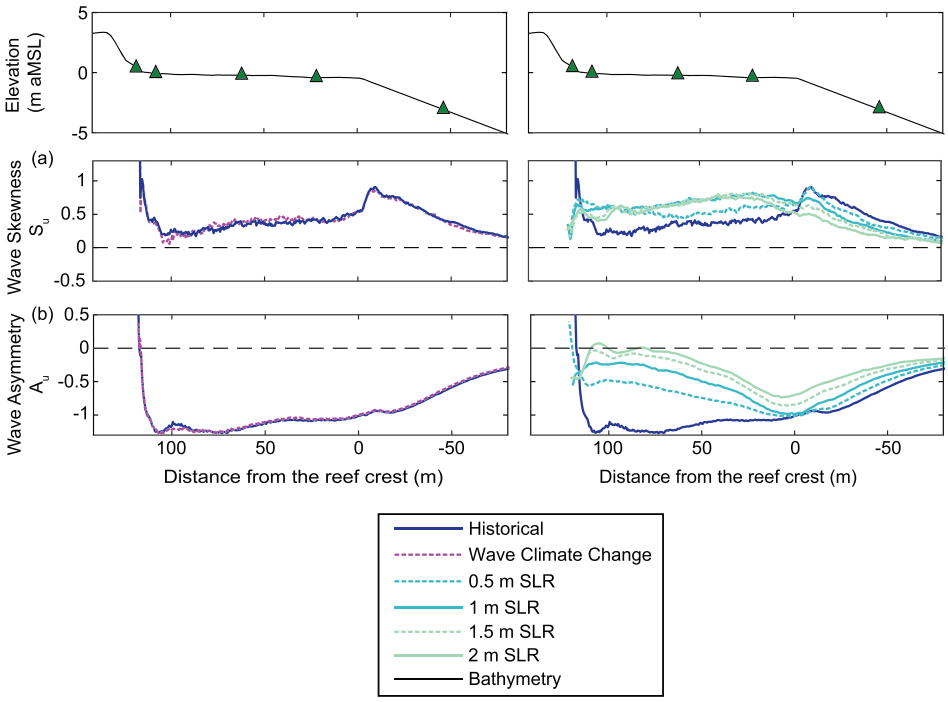

Figure 7. Mean wave skewness and asymmetry from modeled wave motions for the six model scenarios. Left hand column shows Historical and Wave Climate Change scenarios, and the right hand column shows the 4 SLR scenarios with the Historical scenario for reference. Green triangles indicate locations sampled in Figures 8–13.

For the Wave Climate Change scenario, the only future changes considered are the projected 12% decrease in incident wave energy and changes to wave period and direction. The change in incident wave energy produces a corresponding decrease in fore reef $H_{s,lf}$ (−12%) and mean water velocity (−11%). However, there was a relatively smaller effect on reef flat $H_{s,lf}$ (−9%) and flow velocities (−2%) (Figure 6), likely because waves on the reef flat are so strongly controlled by water level.

In contrast, the four SLR scenarios result in large changes to hydrodynamics across the reef. With rising sea levels, less incident wave energy is dissipated by breaking on the fore reef and the $H_{s,hf}$ on the reef flat increases (Figure 6e). $H_{s,lf}$ on the beach and reef flat also increase with SLR, though the effect is greatest for the first 1.5 m of SLR, with little subsequent increase up to +2.0 m SLR (Figure 6f). With +2.0 m of SLR, the beach ridge (maximum island elevation) was flooded for 24% of the model runtime across all wave classes, but because the model underestimates mean water level, this is likely an underestimate of the amount of flooding that would occur with this level of SLR. Thus, substantial flooding of the island under ambient wave conditions is likely to initiate between +1.5 and +2.0 m of SLR, assuming constant island morphology. Note that, physical modeling of island response to SLR suggests island oceanfront ridges aggrade with SLR, potentially mitigating flooding hazard over time (Tuck et al., 2019), a morphodynamic effect not simulated in our model. At the reef crest, reduced wave breaking leads to reduced mean offshore flow, whereas on the reef flat the increased wave heights increase the offshore flow (Figure 6). In total, these model results suggest that over the next century SLR will have a much larger impact on the hydrodynamics of Kwajalein Island's reef than the projected reduction in wave heights.

5.2.2. Wave Nonlinearity

The magnitude and net direction of wave-induced shear stress, which directly affects sediment mobilization and bedload transport, depend on both wave height and wave shape. Thus, to better understand how SLR and the projected reduction in offshore wave heights would affect shear stress, we examined high frequency wave skewness and asymmetry (Figure 7). Wave skewness (S_u) indicates increased velocity magnitude under wave crests—for onshore propagating waves, positive skewness means larger but less frequent onshore velocities relative to offshore (Pomeroy et al., 2015). Wave asymmetry (A_u) represents the "saw-toothed" shape of the wave, with negative asymmetry indicating stronger acceleration in the onshore

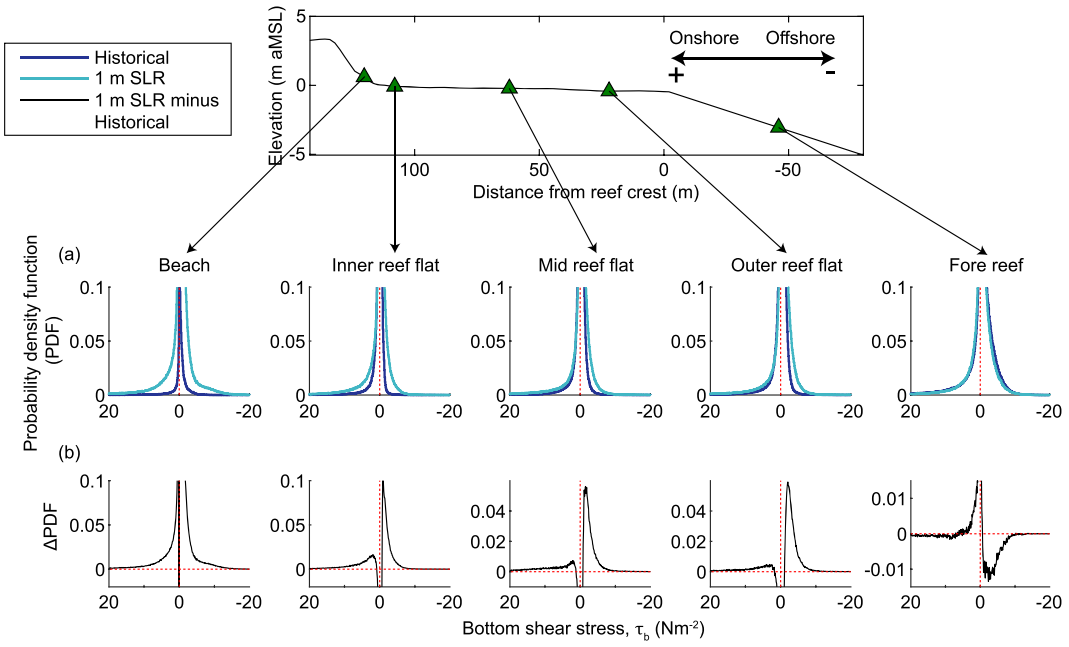

Figure 8. Modeled shear stress probability distributions and their projected change with 1 m SLR. (a) Bottom shear stress for Historical and +1.0 m SLR scenarios and (b) the change in distribution between the two scenarios. The *x* axes of the graphs are flipped to indicate that positive shear stresses are directed onshore. Shear stress was calculated using a skin friction coefficient, $f_{2.5}$, for sediment with median grain diameter $D = 2$ mm.

direction than offshore (Pomeroy et al., 2015). Importantly, wave skewness and asymmetry can diagnose the changes in wave characteristics that drive changes in sediment transport.

Under historical conditions, wave skewness is large and positive (peaked waveforms) on the fore reef but decreases onshore across the reef flat (Figure 7), where high-frequency wave motions are generated primarily by broken wave bores. Wave asymmetry, on the other hand, is negative ("saw-toothed" wave shape) and increases in magnitude from the fore reef to the beach toe (Figure 7), a result of the formation and propagation of broken wave bores across the reef flat.

For the Wave Climate Change scenario, the impact on wave skewness and asymmetry by the decreased incident wave energy is minimal, with slightly reduced S_u and slightly more positive A_u across the reef transect (Figure 7).

However, increasing SLR produces much more substantial changes to wave skewness and asymmetry. S_u decreases roughly linearly with SLR on the fore reef but exhibits nonmonotonic behavior on the reef flat. For +1.0 m of SLR, S_u doubles on the reef flat, but for additional SLR, S_u remains constant or decreases slightly (Figure 7). In contrast, wave asymmetry becomes more positive across the entire reef consistently with SLR. The change is especially pronounced on the reef flat, where the water depth increases and less of the high-frequency wave energy is attributable to broken wave bores (Figure 7). Additionally, after +0.5 m of SLR, A_u peaks over the reef crest and then decreases across the reef flat. By +2.0 m of SLR, high-frequency waves that reach the beach are no longer asymmetric and A_u goes to zero. Thus, trends in the magnitude of wave skewness and wave asymmetry with SLR are opposite-directed. Because wave asymmetry contributes to onshore sediment transport through imbalanced fluid acceleration and wave skewness contributes to onshore sediment transport through imbalanced fluid velocity, SLR alters the relative importance of velocity and acceleration for net sediment transport.

5.2.3. Shear Stress Probability Distributions

Across the atoll's reef, wave skewness and asymmetry contribute to skewed probability distributions of shear stress magnitudes. For the Historical case, offshore-directed mean flow results in shear stress that is more frequently offshore than onshore. However, under positively skewed waves, onshore velocity under the shorter-duration crest is greater in magnitude than offshore velocity under the longer-duration trough.

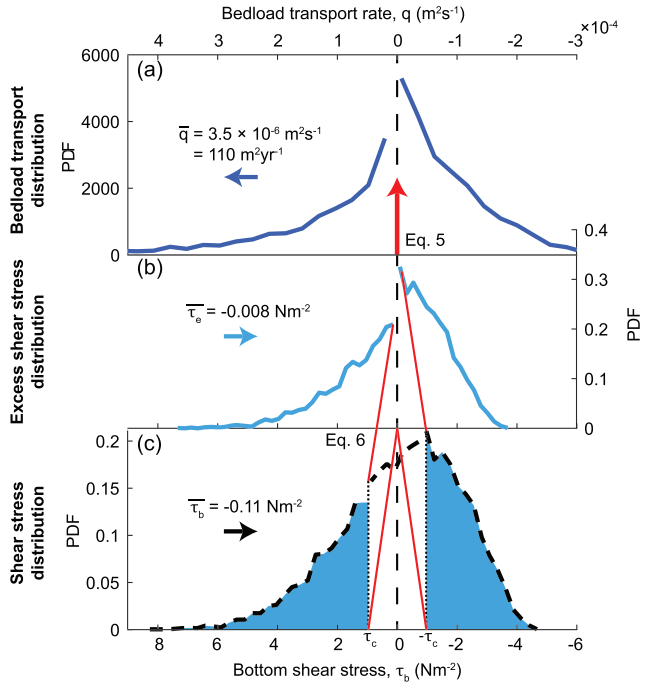

Figure 9. Schematic illustration of the calculation of (a) potential bedload transport for pebble-sized material ($\tau_c \geq 1$ N m^{-2}), given (b) excess shear stress, τ_e, calculated from (c) a hypothetical distribution of near-bottom shear stress, τ_b. Zero values are excluded from the probability distribution functions (PDF) in (a) and (b) for ease of display, but they are included in the calculation of the mean. Mean values and direction are displayed for qualitative illustration.

Additionally, under "saw-toothed" waves (negative A_u), onshore water acceleration is much greater than offshore. Thus, under skewed and asymmetric waves in the Historical scenario, shear stress on the fore reef and reef flat has greater magnitudes in the onshore direction than offshore (Figure 8).

SLR alters shear stress distributions nonuniformly across the reef. SLR inundates the beach to a higher elevation and increases absolute shear stress on the lower portion of the beach that was historically only inundated at high tide. On the reef flat, velocities become more extreme in both onshore and offshore directions with SLR, but on the inner and outer reef flat, increasing wave skewness and H_s compensates for decreasing asymmetry, resulting in shear stress extremes that ultimately remain greater in the onshore direction. On the fore reef, shear stress magnitudes decrease, resulting in a narrower distribution with fewer large onshore outliers (Figure 8). Thus, our model results suggest that with +1.0 m of SLR, mean absolute shear stress increases on the beach toe and across the reef flat by over 400% but decreases on the fore reef by roughly 50%.

5.3. Potential Bedload Sediment Transport

To quantify the net effect wave climate change and SLR are expected to have on net bedload transport rates by the end of the century, we calculated potential bedload flux using the shear stress distributions for the Historical, Wave Climate Change, and all SLR scenarios. The process of estimating bedload transport rates from bottom shear stress is illustrated in Figure 9. Waves only contribute to sediment transport when bottom shear stress magnitudes exceed the critical shear stress (Figure 9c). This threshold results in a contraction of the distribution of τ_e contributing to sediment transport (Figure 9b). Because bedload transport rate varies nonlinearly with shear stress, even if mean τ_b and τ_e are negative, net bedload transport can be positive (Figure 9a). Thus, the extremes in a shear stress distribution influence bedload transport disproportionately more than moderate values. Because wave skewness and asymmetry tend to amplify the positive extremes of the shear stress distribution relative to the negative, wave nonlinearity generally results in net onshore bedload flux.

In the Historical scenario, mean excess shear stress is directed onshore across the entire reef for all sediment size classes, except the largest class at the beach (Figure 10a), resulting in onshore-directed net bedload flux across the reef for all sediment size classes (Figure 10b). Because skin friction increases with grain size, larger grains experience greater shear stress magnitudes and therefore larger potential bedload flux (Figure 10). On the beach, Historical excess shear stress and net bedload flux are nearly 90% lower than on the inner reef flat, which has shear stress and bedload transport values similar to the rest of the reef flat. This suggests that the current reef flat and beach, in combination with modern sea level and wave climate, are in a near steady state configuration (Ortiz & Ashton, 2019).

For higher sea levels, the magnitude of bedload transport on the reef flat and beach increases dramatically, with larger $H_{s,hf}$ and S_u offsetting decreases in wave asymmetry (Figures 6, 7, and 10). This increase in sediment transport is most pronounced for the first +1.0 m of SLR, with less dramatic increases for larger SLR, similar to the trend in S_u. Onshore-directed bedload transport across the reef flat is forecasted to increase 90–280% with just +0.5 m of SLR and 500–900% with +1.0 m of SLR. On the fore reef, for higher SL, bedload flux decreases but remains directed onshore, decreasing in magnitude by 40% for all sediment size classes with +0.5 m of SLR and by 85% with +2.0 m of SLR (Figure 10).

On the reef flat, τ_e increases for +1.0 m of SLR but decreases with further SLR for some grain sizes (Figure 10), a reversal in trend that can be explained by the balance between increasing wave skewness and decreasing wave asymmetry. Wave skewness increases up to +1.0 m of SLR, but asymmetry decreases. Beyond the first +1.0 m of SLR, wave skewness is relatively constant, but wave asymmetry continues decreasing rapidly

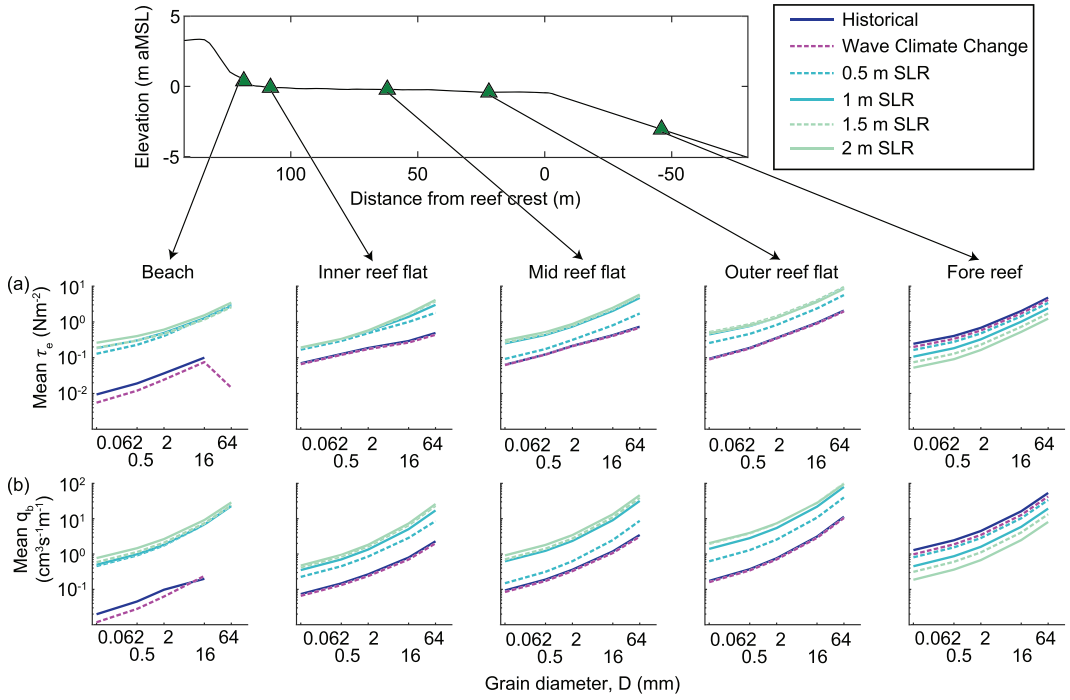

Figure 10. Excess shear stress and net bedload flux for Historical, Wave Climate Change, and four SLR scenarios. (a) Excess shear stress and (b) potential bedload sediment transport rate by grain size and SLR scenario using model velocities sampled at 10 Hz.

(Figure 7). Thus, projected τ_e and q_b are sensitive to the phase lag parameter ϕ_τ (Equation 7), which governs the degree to which flow acceleration, and thus wave asymmetry, contributes to effective bed shear stress. To illustrate this sensitivity, we recomputed bedload transport with ϕ_τ set to each of 0°, 20°, 40°, and 60° (Figure 11). Including the acceleration term ($\phi_\tau > 0$) greatly increases the magnitude of computed bedload transport, suggesting that disregarding the effect of acceleration on sediment transport will dramatically reduce predicted transport magnitudes.

Generally, increasing ϕ_τ increases τ_e and q_b across the reef transect (Figure 11). The absence of a deep bed of sediment in our environment and the presence of natural waves with periods 6–14 s suggest that the appropriate ϕ_τ for this environment should be lower than the 40–60° estimated from u-tube studies with thick beds and short wave periods (3–5 s) (Nielsen, 2006). Using the value most appropriate to our environment of $\phi_\tau = 20°$, q_b on the reef flat and beach toe increases with SLR despite decreases in τ_e between +1.0 and +2.0 m of SLR. However, for higher values of ϕ_τ, the trend of increasing q_b with SLR reverses direction, especially on the beach toe and outer reef flat, for $D \geq 2$ mm (Figure 11). These reversals occur between +0.5 and +1.0 m SLR on the beach and between +1.5 and +2.0 m on the outer reef flat.

5.4. Suspended Sediment Transport Trends

Although most large waves break on the reef crest and only highly diminished waves and wave bores propagate across the reef flat, coarse-grained sediment can still be mobilized and transported in suspended load (Pomeroy et al., 2015). Once sediment is suspended, flow acceleration contributes to sediment momentum, and wave skewness and asymmetry contribute to net transport, its direction quantified as a representative velocity, u_{rep}. Under historical conditions, modeled u_{rep} is directed onshore across the reef flat and the shallow fore reef and is directed offshore over the reef crest, where return flow is strongest, and the outer reef flat (Figure 12). The modeled changes in u_{rep} with wave climate change and SLR are similar to the changes in bedload transport. On the outer reef flat, u_{rep} increases in magnitude and is directed more onshore with increasing SLR (Figure 12). Across most of the fore reef, the sediment advection velocity becomes less onshore directed with increasing SLR. On the inner reef flat, predicted u_{rep} also decreases with increasing SLR, becoming offshore-directed for >1.0 m SLR. The difference in trend direction between the inner and

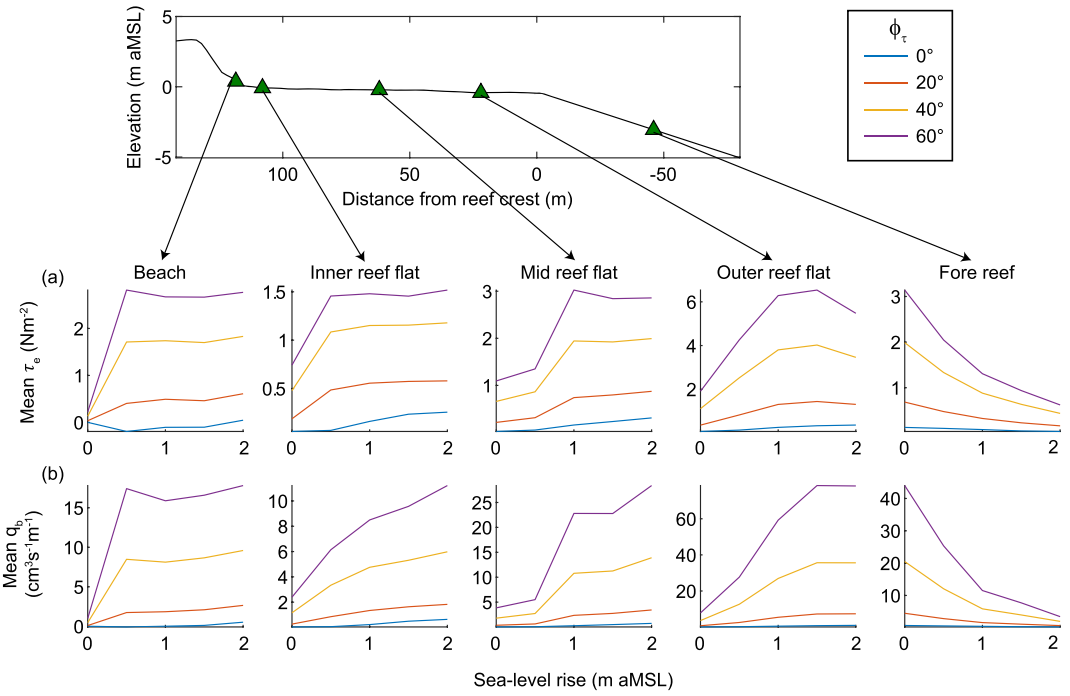

Figure 11. The sensitivity of shear stress and potential bedload transport to flow acceleration. (a) Mean excess shear stress and (b) mean potential bedload sediment transport rate for $D = 2$ mm using model velocities sampled at 10 Hz.

outer reef flat is caused by the tradeoff between increasing wave skewness and decreasing wave asymmetry with SLR. Although S_u increases over the reef flat with SLR, A_u magnitude decreases more steeply on the inner reef flat than the outer (Figure 7). Because S_u and A_u contribute to u_{rep} equally (Equation 11) and in the same direction (onshore), the decreases in A_u magnitude out-pace the increases in S_u on the inner reef flat but not the outer. On the beach, XBeach does not resolve swash-zone processes important for determining suspended sediment transport; thus, we do not interpret trends in suspended sediment transport in this location.

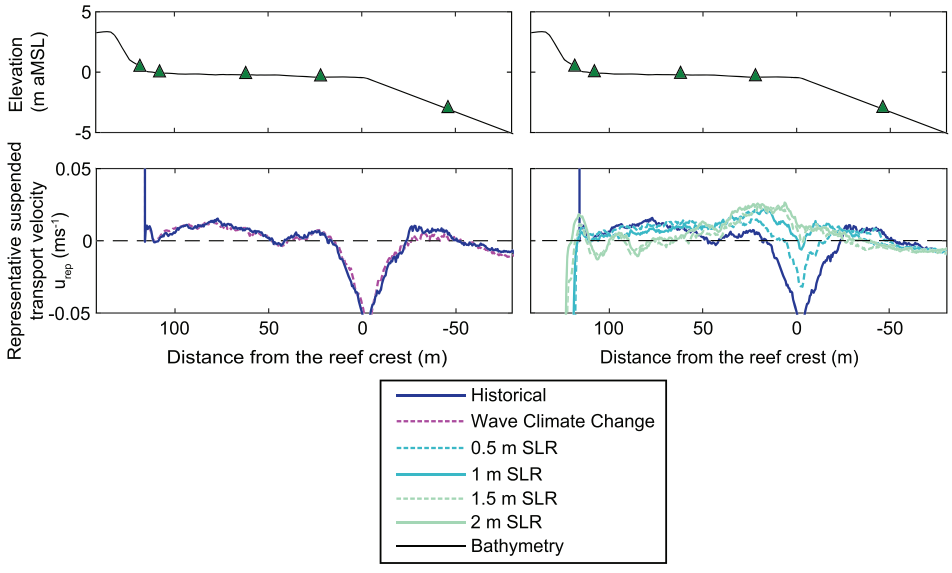

Figure 12. Changes in representative transport velocity, u_{rep}, under six modeling scenarios: Historical and Wave Climate Change scenarios (left panel) and four SLR scenarios with Historical included for reference (right panel).

6. Discussion

6.1. Implications of SLR-Induced Trends in Sediment Transport

The model scenarios allow us to make several inferences about sediment transport processes and how their response to higher sea levels on atoll reefs and beaches similar to those on Kwajalein will change by the end of the century. Most importantly, sediment on the fore reef will be less likely to be transported onto the reef flat than historically, decreasing total sediment volume available for island maintenance, but sediment on the reef flat will be much more likely to be transported onshore to the beach. Thus, SLR may cause erosion of ocean-facing shorelines by starving them of sediment from the fore reef but counter to the inferences made from observations of beach scarping, not through direct offshore transport of beach sediment. Second, the wave climate changes forecasted for Kwajalein Atoll were some of the largest of all locations examined in the Pacific (Shope et al., 2016). Assuming that SLR exceeds +0.5 m across the tropical Pacific Ocean basin by 2100, our modeling suggests that SLR by 2100 will have a significantly larger influence on cross-shore transport than projected wave climate change on atoll reefs across the Pacific. Third, SLR will cause prolonged inundation of the lower beach, enhancing shear stress magnitudes across the subaqueous portion of the beach. From this, we infer an increase in the volume of beach sediment that can be mobilized and greater geomorphological activity of island margins, similar to that projected by Shope and Storlazzi (2019). Fourth, frequent flooding of the island by ambient (nonstorm) waves will occur between +1.5 and +2.0 m of SLR, as noted by Storlazzi et al. (2018). We infer that this flooding will likely move sediment from the beach to the island surface, with this overwash sediment potentially increasing the elevation of the beach ridge with sea level but also resulting in lagoon-ward migration of the island (Tuck et al., 2019).

The net direction and magnitude of morphological changes resulting from SLR-induced alterations to shear stress and potential sediment transport depend on the amount (and thus production that is related to coral reef health) and distribution of sediment on the reef available for transport. For the current Historic conditions, the potential bedload transport decreases substantially from the fore reef to the inner reef flat (Figure 13). However, with +1.0 m of SLR, this gradient reverses direction. If the reef consisted entirely of mobile sediment or if sufficient mobile sediment were present, these flux gradients would suggest a mechanism for the outer reef flat and reef crest to erode. However, most atoll reef flats (including Kwajalein Atoll) are sparsely covered with sediment, confounding straightforward predictions of future morphological change. Additionally, where sediment is produced may also depend on SLR, as SLR moves the point at which waves break shoreward, potentially influencing the spatial distribution of coral growth and erosion. Stating that, currently, the greatest coral growth and thus carbonate production on most coral reefs is on the fore reef. If the availability of sediment for transport correlates with the magnitude of shear stress (i.e., some sediment remains unmobilized at low shear stress), the decreased onshore transport potential from the fore reef to the reef flat would eventually result in a loss of sediment to the reef flat and thus to the island. This effect would be magnified as carbonate production all across the reef is reduced due to the impacts of increasing thermally induced coral bleaching (Hoegh-Guldberg, 1999) and ocean acidification (Pandolfi et al., 2011), potentially threatening the long-term persistence of such islands in the face of sea level rise.

Moving onshore from the fore reef, for +0.5 m SLR, there is a slight minimum of bedload transport between the midreef flat and the inner reef flat, implying the potential for accumulation there. The gradient in bedload transport from the inner reef flat to the beach toe shifts from negative Historically to positive with SLR (Figure 13), suggesting the beach profile may steepen with SLR, though such feedbacks between changes in hydrodynamics and beach morphodynamics were not modeled. The reversals in q_b spatial gradients with SLR should caution against the assumption that atoll island shoreline response will be monotonic with SLR. For example, if onshore transport potential on the reef flat is currently limiting the amount of sediment delivered to an atoll island, net sediment input may increase initially with SLR as onshore transport increases on the reef flat and the transport gradient between the fore reef and reef flat remains negative, resulting in island accretion. However, as onshore potential bedload transport from the fore reef decreases below that on the reef flat with subsequent SLR, net sediment input to the island could decrease, resulting in island erosion. Thus, the initial response of atoll island shorelines to SLR may reverse with additional SLR.

6.2. Broader Implications for Atoll Reef Environments

The windward atoll reef off Kwajalein Island has a relatively steep fore reef and narrow and smooth reef flat. We expect the effects of SLR modeled for Kwajalein to be similar to other atoll reefs with similar geometry,

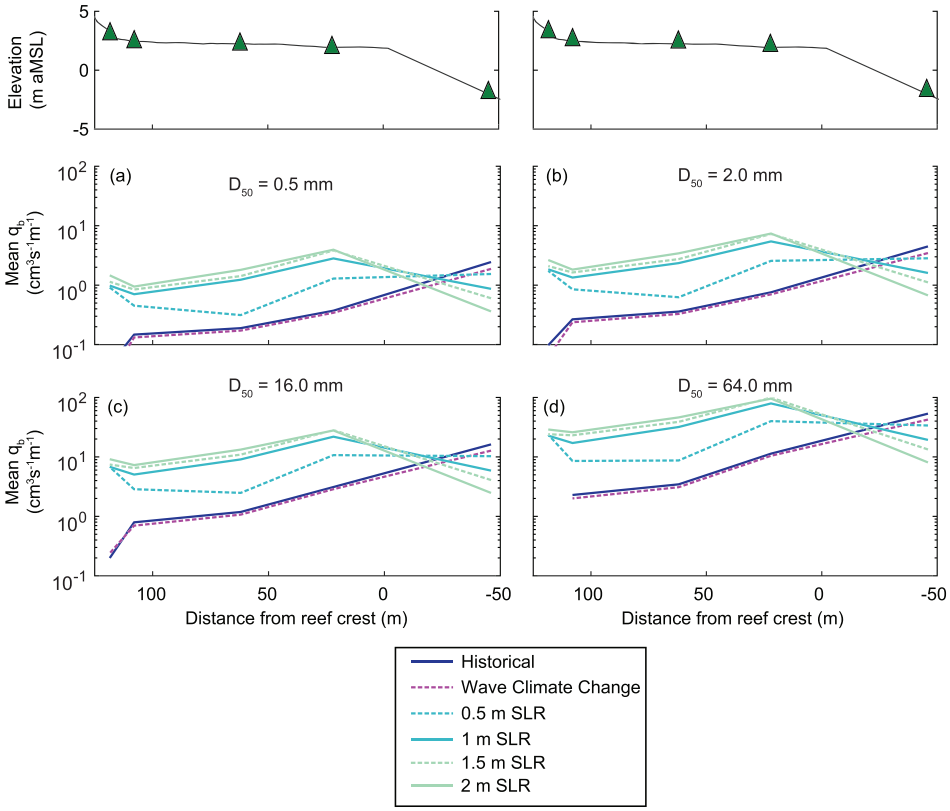

Figure 13. Potential bedload transport across the reef flat and beach for sediment with D_{50} = (a) 0.5, (b) 2.0, (c) 16.0, and (d) 64.0 mm.

especially if they are at similar elevations relative to mean sea level. The decrease in onshore potential transport on the fore reef is driven by decreased bottom shear stress and S_u, whereas the increase in onshore potential sediment transport on the reef flat with SLR is driven by increasing $H_{s,hf}$ and S_u. The response of high frequency wave heights and mean water levels to SLR on atoll reefs is relatively invariant to reef flat width and roughness (Quataert et al., 2015). However, our results demonstrate that wave skewness and onshore potential sediment transport on reef flats increase more slowly with increasing water level. Thus, atoll reefs with deeper reef flats may see lower magnitude increases in onshore transport or even decreases. Additionally, reef flat width, roughness, and fore reef slope determine the dynamics of low-frequency waves on the reef flat, which could produce different trends than in our results. Very wide or rough reef flats can cause smaller $H_{s,lf}$ (e.g., Pomeroy et al., 2018; van Dongeren et al., 2013), because the low-frequency waves are dissipated through friction before interacting with the shoreline to generate standing or resonant waves. Steeper fore reefs tend to generate larger breakpoint-driven low-frequency waves (Quataert et al., 2015). Although the direct contributions of low-frequency wave motions to shear stress and sediment transport are likely small, they modulate $H_{s,hf}$ on the reef flat and beach and flooding of the shoreline (Cheriton et al., 2016). Thus, SLR may increase $H_{s,lf}$ and thus variability in $H_{s,hf}$ and water level on atoll reefs with less steep reefs and rougher or wider reef flats than at Kwajalein Atoll. If SLR increased the duration of resonant or standing low-frequency waves on the reef flat on such reefs, time-mean water surface elevation would also increase, amplifying the increasing trend in onshore potential transport.

By estimating potential sediment transport from instantaneous shear stress, we were able to explore the sensitivity of SLR-driven trends in transport to the influence of flow acceleration relative to velocity. We demonstrated that increasing the influence of flow acceleration tends to increase mean and absolute shear stress across the reef. However, because wave asymmetry and thus mean flow acceleration, decreases with SLR, increasing trends in onshore-directed transport reverse at high SLR when flow acceleration dominates

shear stress distributions. However, the relative magnitude and direction of the trends in potential sediment transport were robust to the relative dominance of flow acceleration for the first +1.0 m of SLR. The tradeoff between wave skewness and wave asymmetry that drives the trend reversals at high SLR suggests a moderating relationship between wave shape and the response of net cross-shore transport to SLR that may be missed by phase-averaged or equilibrium estimates of sediment transport.

The increases in onshore transport on the reef flat and beach outlined here stand in contrast to modeling results for barrier reef island transects, where SLR is predicted to mainly cause beach erosion through offshore transport (Baldock et al., 2015). Unlike atoll island beaches, barrier reef island beaches are often continuous with a sandy shoreface that extends into a back-reef lagoon, and waves that break on the shallow barrier reef flat can reform in the deeper lagoon waters. Thus, both the character of waves that reach the shoreline and the malleability of the shoreface profile distinguish barrier reef islands from the atoll reef considered here. However, although the modeled barrier reef islands tended to erode with SLR through Bruun rule-style offshore transport, there were reef geometries where accretion occurred instead, and those included barrier reefs with shallow, narrow reef flats like that considered here and narrow back-reef lagoons (Baldock et al., 2015). Future research contrasting cross-reef sediment transport between these two environments may be warranted.

6.3. Model Limitations

We emphasize that we use the two measures of sediment transport, q_b and u_{rep}, only as proxies for transport rates. In particular, q_b scales with shear stress in excess of a mobilization threshold. However, Kench and McLean (1996) demonstrated that for nonspherical bioclastic carbonate sediment, the mobilization threshold can be lower than that predicted by the critical Shield's parameter. Additionally, in an environment where sediment is sparse, that is, the Kwajalein Island reef flat, isolated sediment grains or small collections of grains not interlocking with a bed of sediment would experience lower stabilizing frictional force, resulting in a lower mobilization threshold (Aubert et al., 2016) and potentially different friction coefficient values. Wave streaming is neglected in Equation 5, the effect of which is likely underestimation of onshore transport on the fore reef and reef flat. Also, above some shear stress threshold, all sediment size classes are mobilized and a more sophisticated transport parameterization would be required to account for interparticle interactions and suspended sediment-flow feedbacks (Smit et al., 2010). Additionally, u_{rep} was tuned for low-gradient, sandy beaches, and it assumes a particular balance between wave asymmetry and skewness that could be weighted differently for different topography or sediment characteristics, though we assume that a proper calibration of u_{rep} for our environment will not change with SLR.

Recent numerical modeling of idealized geometries has demonstrated that for reefs with finite length protruding from a straight coast, refraction from the lateral edges of the reef can increase wave heights at the center of reef flats relative to what 1-D wave models would predict (Baldock et al., 2020). This effect is limited for shallow, narrow reef flats like that studied here but becomes more pronounced for deeper reef flats or with SLR. Along the particular reef transect where we deployed wave sensors, such an effect could arise from the curving coastline to the south, resulting in refracted wave inputs from the southwest on the reef flat. With SLR, refraction would increase wave height and orbital velocity on the midreef flat, enhancing the trend of increasing onshore transport predicted by our model for that location. Thus, our results may underestimate potential cross-shore sediment transport on the midinner reef flat.

Additionally, SLR-induced changes to refraction would alter longshore transport gradients and influence readjustment of atoll reef island shorelines. Modeling by Shope et al. (2017) and Shope and Storlazzi (2019) found that SLR would enhance existing longshore transport gradients and patterns of erosion and accretion across atolls. In contrast, for salients on fringing reefs distinct from atoll reefs, Baldock et al. (2019) predicted that SLR-induced changes to refraction would drive erosion, reducing longshore shoreline variability. Additionally, as longshore transport rates, overwash rates, and sediment inputs change with SLR, so would the geometry of the reef flat-beach transect. If the atoll island shoreline retreated, the reef flat would widen, modulating $H_{s,lf}$ as discussed in section 6.2. The beach profile itself would adjust rapidly to changing forcing, such that q_b on the beach might not change as drastically as predicted by our model, which did not simulate island morphodynamics. Any prediction of total shoreline response to SLR would need to incorporate alongshore-variable effects and morphodynamic coupling in addition to changes in sediment inputs from the reef and sediment export from the beach through overwash.

7. Conclusions

In this study, we used forecasts of wave climate change from a global climate model ensemble and numerical modeling of hydrodynamics and wave propagation over an atoll reef to predict changes in potential cross-shore transport likely to occur due to SLR and wave climate change. The climate model ensemble forecasted a 12% reduction in wave energy incident on the reef at Kwajalein Island by the end of the century, equivalent to a reduction of one standard deviation of annual mean wave energy in the instrumental record. However, compared to SLR, this marked change in wave energy had negligible impact on the hydrodynamics and potential sediment transport across the reef.

Our numerical model analysis predicts that with rising water level, the magnitude of net onshore potential bedload transport on the fore reef, where the vast majority of sediment production on a reef occurs, decreases substantially due to reduced wave nonlinearity and bottom shear stress. However, on the reef flat, potential bedload transport increases in the onshore direction with rising sea level. Analysis of the hydrodynamics driving cross-shore transport revealed that on the shallow atoll reef flat, the response of cross-shore sediment transport to SLR is mediated by a tradeoff between increasing wave skewness and decreasing wave asymmetry. For higher SLR values, skewness becomes constant, but asymmetry continues decreasing, which can generate reversals in the trend of increasingly onshore shear stress and bedload transport for higher values of SLR.

Reduced carbonate sediment production due to the impacts of increasing thermally induced coral bleaching and ocean acidification, together with the opposing trends in transport between the fore reef and reef flat identified here, suggests that the island beach will receive fewer sediment inputs from the fore reef and that with SLR, net erosion of the islands will likely occur. Predicting the morphological evolution of a particular island due to SLR requires incorporation of both existing and forecasted local sediment production and coupling between sediment transport processes and morphological evolution of the reef under sea level rise and global stressors such as coral bleaching and ocean acidification.

Data Availability Statement

The wave and water level data used to calibrate and validate the XBeach model can be found in the USGS ScienceBase (https://doi.org/10.5066/P9RYN5NH). The MATLAB code used to run XBeach and plot the figures in this manuscript can be found in the Woods Hole Open Access Server at https://hdl.handle.net/1912/24795 (https://doi.org/10.26025/1912/24795). XBeach and the XBeach toolbox for MATLAB are open source and can be found at https://oss.deltares.nl/web/xbeach website.

Acknowledgments

This study was supported by the Strategic Environmental Research and Development Program through awards SERDP: RC-2334, and RC-2336. Any use of trade, firm, or product names is for descriptive purposes only and does not imply endorsement by the U.S. Government.

References

Albert, S., Leon, J. X., Grinham, A. R., Church, J. A., Gibbes, B. R., & Woodroffe, C. D. (2018). Interactions between sea-level rise and wave exposure on reef island dynamics in the Solomon Islands. *Environmental Research Letters*, *11*, 054011. https://doi.org/10.1088/1748-9326/11/5/054011

Aubert, G., Langlois, V. J., & Allemand, P. (2016). Bedrock incision by bedload: Insights from direct numerical simulations. *Earth Surface Dynamics*, *4*, 327–342. https://doi.org/10.5194/esurf-4-327-2016

Baldock, T. E., Golshani, A., Atkinson, A., Shimamoto, T., Wu, S., Callaghan, D. P., & Mumby, P. J. (2015). Impact of sea-level rise on cross-shore sediment transport on fetch-limited barrier reef island beaches under modal and cyclonic conditions. *Marine Pollution Bulletin*, *97*, 188–198. https://doi.org/10.1016/j.marpolbul.2015.06.017

Baldock, T. E., Shabani, B., & Callaghan, D. P. (2019). Open access Bayesian belief networks for estimating the hydrodynamics and shoreline response behind fringing reefs subject to climate changes and reef degradation. *Environmental Modelling & Software*, *119*, 327–340. https://doi.org/10.1016/j.envsoft.2019.07.001

Baldock, T. E., Shabani, B., Callaghan, D. P., Hu, Z., & Mumby, P. J. (2020). Two-dimensional modelling of wave dynamics and wave forces on fringing coral reefs. *Coastal Engineering*, *155*, 103594. https://doi.org/10.1016/j.coastaleng.2019.103594

Becker, J. M., Merrifield, M. A., & Yoon, H. (2016). Infragravity waves on fringing reefs in the tropical Pacific: Dynamic setup. *Journal of Geophysical Research: Oceans*, *121*, 3010–3028. https://doi.org/10.1002/2015JC011516

Bergillos, R. J., Masselink, G., & Ortega-Sánchez, M. (2017). Coupling cross-shore and longshore sediment transport to model storm response along a mixed sand-gravel coast under varying wave directions. *Coastal Engineering*, *129*, 93–104. https://doi.org/10.1016/j.coastaleng.2017.09.009

Cheriton, O. M., Storlazzi, C. D., & Rosenberger, K. J. (2016). Observations of wave transformation over a fringing coral reef and the importance of low-frequency waves and offshore water levels to runup, overwash, and coastal flooding. *Journal of Geophysical Research: Oceans*, *121*, 3121–3140. https://doi.org/10.1002/2015JC011231

Church, J. A., Clark, P. U., Cazenave, S., Gregory, J. M., Jevrejeva, S., Levermann, A., et al. (2013). Chapter 13: Sea level change. In T. F. Stocker, et al., (Eds.), *Climate change 2013: The physical science basis. Contribution of Working Group I to the Fifth Assessment Report of the Intergovernmental Panel on Climate Change* (pp. 1139–1177). Cambridge, UK, and New York, NY: Cambridge University Press.

Church, J. A., & White, N. J. (2006). A 20th century acceleration in global sea-level rise. *Geophysical Research Letters*, *33*, L01602. https://doi.org/10.1029/2005GL024826

Damgaard, J. S., Whitehouse, R. J. S., & Soulsby, R. L. (1997). Bed-load sediment transport on steep longitudinal slopes. *Journal of Hydraulic Engineering*, *123*(12), 1130–1138. https://doi.org/10.1061/(ASCE)0733-9429(1997)123:12(1130)

Dawson, J. L., & Smithers, S. G. (2010). Shoreline and beach volume change between 1967 and 2007 at Raine Island, Great Barrier Reef, Australia. *Global and Planetary Change*, *72*, 141–154. https://doi.org/10.1016/j.gloplacha.2010.01.026

Dickinson, W. R. (1999). Holocene sea-level record on Funafuti and potential impact of global warming on Central Pacific atolls. *Quaternary Research*, *51*(2), 124–132. https://doi.org/10.1006/qres.1998.2029

Dickinson, W. R. (2009). Pacific atoll living: How long already and until when? *GSA Today*, *19*(3), 4–10. https://doi.org/10.1130/GSATG35A.1

Ford, M. R. (2013). Shoreline changes interpreted from multi-temporal aerial photographs and high resolution satellite images: Wotje Atoll, Marshall Islands. *Remote Sensing of Environment*, *135*, 130–140. https://doi.org/10.1016/j.rse.2013.03.027

Ford, M. R., & Kench, P. S. (2015). Multi-decadal shoreline changes in response to sea-level rise in the Marshall Islands. *Anthropocene*, *11*, 14–24. https://doi.org/10.1016/j.ancene.2015.11.002

Ford, M. R., & Kench, P. S. (2016). Spatiotemporal variability of typhoon impacts and relaxation intervals on Jaluit Atoll, Marshall Islands. *Geology*, *44*, 159–162. https://doi.org/10.1130/G37402.1

Gawehn, M., van Dongeren, A., van Rooijen, A., Storlazzi, C. D., Cheriton, O. M., & Reniers, A. (2016). Identification and classification of very low frequency waves on a coral reef flat. *Journal of Geophysical Research: Oceans*, *121*, 7560–7574. https://doi.org/10.1002/2016JC011834

Grossman, E. E., Fletcher, C. H. III, & Richmond, B. M. (1998). The Holocene sea-level highstand in the equatorial Pacific: Analysis of the insular paleosea-level database. *Coral Reefs*, *17*(3), 309–327. https://doi.org/10.1007/s003380050132

Harris, D. L., Rovere, A., Casella, E., Power, H., Canavesio, R., Collin, A., et al. (2018). Coral reef structural complexity provides important coastal protection from waves under rising sea levels. *Science Advances*, *4*, eaao4350. https://doi.org/10.1126/sciadv.aao4350

Hoegh-Guldberg, O. (1999). Climate change, coral bleaching and the future of the world's coral reefs. *Marine and Freshwater Research*, *50*, 839–866.

Hoeke, R. K., McInnes, K. L., Kruger, J. C., McNaught, R. J., Hunter, J. R., & Smithers, S. G. (2013). Widespread inundation of Pacific islands triggered by distant-source wind-waves. *Global and Planetary Change*, *108*, 128–138. https://doi.org/10.1016/j.gloplacha.2013.06.006

Hsu, C. W., & Velicogna, I. (2017). Detection of sea level fingerprints derived from GRACE gravity data. *Geophysical Research Letters*, *44*, 8953–8961. https://doi.org/10.1002/2017GL074070

Huang, N. E., & Wu, Z. (2008). A review on Hilbert-Huang transform: Method and its applications to geophysical studies. *Reviews of Geophysics*, *46*, 2007RG000228. https://doi.org/10.1029/2007RG000228

Hunt, Jr C., Spengler, S., & Gingerich, S. (1995). Lithological influences on freshwater lens geometry and aquifer tidal response at Kwajalein atoll. In *Proceedings of the American Water Resources Association Symposium*, 267-276. AWRA

Joint Typhoon Warning Center (JTWC) (1988). *1988 Annual Tropical Cyclone Report*. Guam: United States Joint Typhoon Warning Center.

Joint Typhoon Warning Center (JTWC) (1991). *1991 Annual Tropical Cyclone Report*. Guam: United States Joint Typhoon Warning Center.

Kench, P., Smithers, S., & McLean, R. (2012). Rapid reef island formation and stability over an emerging reef flat: Bewick Cay, northern Great Barrier Reef, Australia. *Geology*, *40*(4), 347–350. https://doi.org/10.1130/G32816.1

Kench, P. S., & Brander, R. W. (2006). Response of reef island shorelines to seasonal climate oscillations: South Maalhosmadulu atoll, Maldives. *Journal of Geophysical Research*, *111*, F01001. https://doi.org/10.1029/2005JF000323

Kench, P. S., & Cowell, P. J. (2001). The morphological response of atoll islands to sea-level rise. Part 2: Application of the modified shoreline translation model (STM). *Journal of Coastal Research*, *SI34*, 645–656.

Kench, P. S., & McLean, R. F. (1996). Hydraulic characteristics of bioclastic deposits: New possibilities for environmental interpretation using settling velocity fractions. *Sedimentology*, *43*(3), 561–570. https://doi.org/10.1046/j.1365-3091.1996.d01-23.x

Kench, P. S., Owen, S. D., & Ford, M. R. (2014). Evidence for coral island formation during rising sea level in the central Pacific Ocean. *Geophysical Research Letters*, *41*, 820–827. https://doi.org/10.1002/2013GL059000

Komar, P. D., & Miller, M. C. (1975). On the comparison between the threshold of sediment motion under waves and unidirectional currents with a discussion of the practical evaluation of the threshold. *Journal of Sedimentary Research*, *45*, 362–367. https://doi.org/10.1306/212F6D66-2B24-11D7-8648000102C1865D

Kopp, R. E., DeConto, R. M., Bader, D. A., Hay, C. C., Horton, R. M., Kulp, S., et al. (2017). Evolving understanding of Antarctic ice-sheet physics and ambiguity in probabilistic sea-level projections. *Earth's Future*, *5*, 1217–1233. https://doi.org/10.1002/2017EF000663

Kopp, R. E., Horton, R. M., Little, C. M., Mitrovica, J. X., Oppenheimer, M., Rasmussen, D. J., et al. (2014). Probabilistic 21st and 22nd century sea-level projections at a global network of tide-gauge sites. *Earth's Future*, *2*, 383–406. https://doi.org/10.1002/2014EF000239

Lashley, C. H., Roelvink, D., van Dongeren, A., Buckley, M. L., & Lowe, R. J. (2018). Nonhydrostatic and surfbeat model predictions of extreme wave run-up in fringing reef environments. *Coastal Engineering*, *137*, 11–27. https://doi.org/10.1016/j.coastaleng.2018.03.007

McLean, R., & Kench, P. (2015). Destruction or persistence of coral atoll islands in the face of 20th and 21st century sea level rise? *Wiley Interdisciplinary Reviews: Climate Change*, *6*, 445–463. https://doi.org/10.1002/wcc.350

Merrifield, M., Becker, J., Ford, M., & Yao, Y. (2014). Observations and estimates of wave-driven water level extremes at the Marshall Islands. *Geophysical Research Letters*, *41*, 7245–7253. https://doi.org/10.1002/2014GL061005

Mitrovica, J. X., Gomez, N., & Clark, P. U. (2009). The sea-level fingerprint of West Antarctic collapse. *Science*, *323*(5915), 753. https://doi.org/10.1126/science.1166510

Montaggioni, L. F. (2005). History of Indo-Pacific coral reef systems since the last glaciation: Development patterns and controlling factors. *Earth Science Reviews*, *71*(1–2), 1–75. https://doi.org/10.1016/j.earscirev.2005.01.002

Nielsen, P. (2006). Sheet flow sediment transport under waves with acceleration skewness and boundary layer streaming. *Coastal Engineering*, *53*(9), 749–758. https://doi.org/10.1016/j.coastaleng.2006.03.006

Nielsen, P., & Callaghan, D. P. (2003). Shear stress and sediment transport calculations for sheet flow under waves. *Coastal Engineering*, *47*(3), 347–354. https://doi.org/10.1016/S0378-3839(02)00141-2

Oberle, F. K. J., Swarzenski, P. W., & Storlazzi, C. D. (2017). Atoll groundwater movement and its response to climatic and sea-level fluctuations. *Watermark*, *9*, 650. https://doi.org/10.3390/w9090650

Ortiz, A., & Ashton, A. D. (2019). Exploring carbonate reef flat hydrodynamics and potential formation and growth mechanisms for motu. *Marine Geology*, *412*, 173–186. https://doi.org/10.1016/j.margeo.2019.03.005

Pandolfi, J. M., Connolly, S. R., Marshall, D. J., & Cohen, A. L. (2011). Projecting coral reef futures under global warming and ocean acidification. *Science*, *333*(6041), 418–422. https://doi.org/10.1126/science.1204794

Pender, D., & Karunarathna, H. (2013). A statistical-process based approach for modelling beach profile variability. *Coastal Engineering*, *81*, 19–29. https://doi.org/10.1016/j.coastaleng.2013.06.006

Perry, C., Kench, P., Smithers, S., Riegl, B., Yamano, H., & O'Leary, M. (2011). Implications of reef ecosystem change for the stability and maintenance of coral reef islands. *Global Change Biology*, *17*(12), 3679–3696. https://doi.org/10.1111/j.1365-2486.2011.02523.x

Pomeroy, A. W., Lowe, R. J., van Dongeren, A. R., Ghisalberti, M., Bodde, W., & Roelvink, D. (2015). Spectral wave-driven sediment transport across a fringing reef. *Coastal Engineering*, *98*, 78–94. https://doi.org/10.1016/j.coastaleng.2015.01.005

Pomeroy, A. W. M., Lowe, R. J., Ghisalberti, M., Storlazzi, C., Symonds, G., & Roelvink, D. (2017). Sediment transport in the presence of large reef bottom roughness. *Journal of Geophysical Research: Oceans*, *122*, 1347–1368. https://doi.org/10.1002/2016JC011755

Pomeroy, A. W. M., Lowe, R. J., Ghisalberti, M., Winter, G., Storlazzi, C., & Cuttler, M. (2018). Spatial variability of sediment transport processes over intratidal and subtidal timescales within a fringing coral reef system. *Journal of Geophysical Research: Earth Surface*, *123*, 1013–1034. https://doi.org/10.1002/2017JF004468

Quataert, E. (2015). Wave runup on atoll reefs. Masters thesis. Delft University of Technology, Delft, Netherlands.

Quataert, E., Storlazzi, C., van Rooijen, A., Cheriton, O., & van Dongeren, A. (2015). The influence of coral reefs and climate change on wave-driven flooding of tropical coastlines. *Geophysical Research Letters*, *42*, 6407–6415. https://doi.org/10.1002/2015GL064861

Rankey, E. C. (2011). Nature and stability of atoll island shorelines: Gilbert island chain, Kiribati, equatorial Pacific. *Sedimentology*, *58*(7), 1831–1859. https://doi.org/10.1111/j.1365-3091.2011.01241.x

Ruessink, B. G., Ramaekers, G., & van Rijn, L. C. (2012). On the parameterization of the free-stream non-linear wave orbital motion in nearshore morphodynamic models. *Coastal Engineering*, *65*, 56–63. https://doi.org/10.1016/j.coastaleng.2012.03.006

Sheppard, C., Dixon, D. J., Gourlay, M., Sheppard, A., & Payet, R. (2005). Coral mortality increases wave energy reaching shores protected by reef flats: Examples from the Seychelles. *Estuarine, Coastal and Shelf Science*, *64*(2–3), 223–234. https://doi.org/10.1016/j.ecss.2005.02.016

Shope, J. B., & Storlazzi, C. D. (2019). Assessing morphologic controls on atoll island alongshore sediment transport gradients due to future sea-level rise. *Frontiers in Marine Science*, *6*, 245. https://doi.org/10.3389/fmars.2019.00245

Shope, J. B., Storlazzi, C. D., Erikson, L. H., & Hegermiller, C. A. (2016). Changes to extreme wave climates of islands within the western tropical pacific throughout the 21st century under RCP 4.5 and RCP 8.5, with implications for island vulnerability and sustainability. *Global and Planetary Change*, *141*, 25–38. https://doi.org/10.1016/j.gloplacha.2016.03.009

Shope, J. B., Storlazzi, C. D., & Hoeke, R. K. (2017). Projected atoll shoreline and run-up changes in response to sea-level rise and varying large wave conditions at Wake and Midway Atolls, Northwestern Hawaiian Islands. *Geomorphology*, *295*, 537–550. https://doi.org/10.1016/j.geomorph.2017.08.002

Smit, P. B., Stelling, G. S., Roelvink, D., van Thiel de Vries, J., McCall, R., van Dongeren, A., et al. (2010). *XBeach: Non-Hydrostatic Model: Validation, Verification, and Model Description*. Delft, Netherlands: Delft University of Technology.

Soulsby, R. L., & Damgaard, J. S. (2005). Bedload sediment transport in coastal waters. *Coastal Engineering*, *52*, 673–689. https://doi.org/10.1016/j.coastaleng.2005.04.003

Spennemann, D. H. R. (2004). Typhoons in Micronesia: A History of Tropical Cyclones and Their Effects until 1914. Saipan, Commonwealth of the Northern Mariana Islands: Division of Historic Preservation, 2004. ISBN:1-878453-79-3

Storlazzi, C. D., Elias, E. P. L., & Berkowitz, P. (2015). Many atolls may be uninhabitable within decades due to climate change. *Scientific Reports*, *5*, 14546. https://doi.org/10.1038/srep14546

Storlazzi, C. D., Gingerich, S. B., van Dongeren, A., Cheriton, O. M., Swarzenski, P. W., Quataert, E., et al. (2018). Most atolls will be uninhabitable by the mid-21st century because of sea-level rise exacerbating wave-driven flooding. *Science Advances*, *4*, eaap9741. https://doi.org/10.1126/sciadv.aap9741

Storlazzi, C. D., Shope, J. B., Erikson, L. H., Hegermiller, C., & Barnard, P. (2015). Future wave and wind projections for United States and United States-affiliated Pacific islands. U.S. Geological Survey Open-File Report 2015–1001. doi:https://doi.org/10.3133/ofr20151001

Sugerman, B. B. (1972). Insects and other arthropods from Kwajalein Atoll (Marshall Islands). *Proceedings of the Hawaiian Entomological Society*, *21*, 271–286.

Symonds, G., Huntley, D. A., & Bowen, A. J. (1982). Two-dimensional surf beat: Long wave generation by a time-varying breakpoint. *Journal of Geophysical Research*, *87*(C1), 492–498. https://doi.org/10.1029/JC087iC01p00492

Tuck, M. E., Ford, M. R., Masselink, G., & Kench, P. S. (2019). Physical modelling of reef island topographic response to rising sea levels. *Geomorphology*, *345*, 106833. https://doi.org/10.1016/j.geomorph.2019.106833

Van Dongeren, A., Lowe, R., Pomeroy, A., Trang, D. M., Roelvink, D., Symonds, G., & Ranasinghe, R. (2013). Numerical modeling of low-frequency wave dynamics over a fringing coral reef. *Coastal Engineering*, *73*, 178–190. https://doi.org/10.1016/j.coastaleng.2012.11.004

van Thiel de Vries, J. (2009). Dune erosion during storm surges. PhD thesis. Delft University of Technology., Delft, Netherlands.

Webb, A. P., & Kench, P. S. (2010). The dynamic response of reef islands to sea-level rise: Evidence from multi-decadal analysis of island change in the central pacific. *Global and Planetary Change*, *72*(3), 234–246. https://doi.org/10.1016/j.gloplacha.2010.05.003

Woodroffe, C. D. (2008). Reef-island topography and the vulnerability of atolls to sea-level rise. *Global and Planetary Change*, *62*, 77–96. https://doi.org/10.1016/j.gloplacha.2007.11.001

Wu, Z., & Huang, N. E. (2009). Ensemble empirical mode decomposition: A noise-assisted data analysis method. *Advances in Adaptive Data Analysis*, *01*(01), 1–41. https://doi.org/10.1142/S1793536909000047

Xu, R., & Wunsch, D. II (2005). Survey of clustering algorithms. *IEEE Transactions on Neural Networks*, *16*(3), 645–678. https://doi.org/10.1109/TNN.2005.845141

Zhang, L., Karnauskas, K. B., Donnelly, J. P., & Emanuel, K. (2017). Response of the North Pacific tropical cyclone climatology to global warming: Application of dynamical downscaling to CMIP5 models. *Journal of Climate*, *30*, 1233–1243. https://doi.org/10.1175/JCLI-D-16-0496.1